

Vertically resolved magma ocean–protoatmosphere evolution: H₂, H₂O, CO₂, CH₄, CO, O₂, and N₂ as primary absorbers

TIM LICHTENBERG ¹, DAN J. BOWER ², MARK HAMMOND ³, RYAN BOUKROUCHE ¹, PATRICK SANAN ⁴,
SHANG-MIN TSAI ¹ AND RAYMOND T. PIERREHUMBERT ¹

¹ *Atmospheric, Oceanic and Planetary Physics, Department of Physics, University of Oxford, United Kingdom*

² *Center for Space and Habitability, University of Bern, Switzerland*

³ *Department of the Geophysical Sciences, University of Chicago, USA*

⁴ *Institute of Geophysics, Department of Earth Sciences, ETH Zurich, Switzerland*

Journal of Geophysical Research: Planets, *Exoplanets: The Nexus of Astronomy and Geoscience*, doi: [10.1029/2020JE006711](https://doi.org/10.1029/2020JE006711)

ABSTRACT

The earliest atmospheres of rocky planets originate from extensive volatile release during magma ocean epochs that occur during assembly of the planet. These establish the initial distribution of the major volatile elements between different chemical reservoirs that subsequently evolve via geological cycles. Current theoretical techniques are limited in exploring the anticipated range of compositional and thermal scenarios of early planetary evolution, even though these are of prime importance to aid astronomical inferences on the environmental context and geological history of extrasolar planets. Here, we present a coupled numerical framework that links an evolutionary, vertically-resolved model of the planetary silicate mantle with a radiative-convective model of the atmosphere. Using this method we investigate the early evolution of idealized Earth-sized rocky planets with end-member, clear-sky atmospheres dominated by either H₂, H₂O, CO₂, CH₄, CO, O₂, or N₂. We find central metrics of early planetary evolution, such as energy gradient, sequence of mantle solidification, surface pressure, or vertical stratification of the atmosphere, to be intimately controlled by the dominant volatile and outgassing history of the planet. Thermal sequences fall into three general classes with increasing cooling timescale: CO, N₂, and O₂ with minimal effect, H₂O, CO₂, and CH₄ with intermediate influence, and H₂ with several orders of magnitude increase in solidification time and atmosphere vertical stratification. Our numerical experiments exemplify the capabilities of the presented modeling framework and link the interior and atmospheric evolution of rocky exoplanets with multi-wavelength astronomical observations.

PLAIN LANGUAGE SUMMARY

The climate and surface conditions of rocky planets are sensitive to the composition of their atmospheres, but the origins of these atmospheres remain unknown. During the final stages of planetary accretion, when the whole of the planet solidifies from lava to solid rock, volatiles can rapidly cycle between interior and atmosphere, and control the cooling properties of the planet. In order to understand how cooling planets with different volatile compositions evolve, we use computer simulations to analyze their thermal evolution, outgassing, and observable signatures. We find the planetary cooling sequence to differ by orders of magnitude depending on the primary volatile. CO, N₂, and O₂ rapidly outgas, but allow planets to solidify efficiently. H₂O, CO₂, and CH₄ build an intermediate class with substantially delayed cooling, but varying outgassing rate. H₂ most efficiently inhibits solidification relative to the other cases. All considered volatiles show distinctive evolution of the atmosphere and interior and display different atmospheric signals that can be measured by astronomical surveys. Deviations in the geological properties of the planetary interior similarly manifest in the atmospheric signal. Future observations may isolate distinctive features in exoplanet atmospheres to infer interior state and composition.

1. INTRODUCTION

The debate surrounding the formation and long-term evolution of rocky planets has been dominated by the wealth of data obtained from the terrestrial planets and planetary materials in the Solar System. However, current and upcoming astronomical surveys of planet-forming circumstellar disks and evolved extrasolar planets will increase the available data greatly. For instance, astrochemical studies of ever-higher precision deliver clues to the origins of major atmophile elements during the main planet formation era (van 't Hoff et al. 2020; Bergner et al. 2020). Ongoing (Ricker et al. 2015; Dreizler et al. 2020) and future (Gaudi et al. 2020; Meixner et al. 2019; The LUVUOIR Team 2019; Apai et al. 2019; Quanz et al. 2019) exoplanet surveys will reveal statistically meaningful characteristics of Earth-sized planets on temperate orbits. Having so far only glimpsed the richness and diversity of the exoplanet census, statistical evaluation of basic physical properties—such as mass, radius, and atmospheric features—teach us that individual rocky planets differ substantially from one another and from the terrestrial planets of the Solar System (Jontof-Hutter 2019; Pierrehumbert & Hammond 2019; Owen 2019). Shaped by extreme post-accretionary processes, the impinging radiation of close-in planets can strip away their volatile envelopes, leaving only dessicated, bare rocks (Owen & Wu 2013; Lopez & Fortney 2014; Jin et al. 2014; Fulton et al. 2017), with permanent day- and nightsides (Kreidberg et al. 2019) or in eternal runaway greenhouse states (Turbet et al. 2019). Further out, being born from volatile-rich building blocks, solid-dominated planets may resemble scaled-up versions of the icy moons of the outer Solar System (Kuchner 2003; Léger et al. 2004), where high-pressure ice phases at the mantle-atmosphere interface inhibit Earth-like geochemical cycling of nutrients (Noack et al. 2017; Kite & Ford 2018; Journaux et al. 2020). For the more massive super-Earths, the crushing pressures at depth generate a supercritical fluid of equilibrated vapor and rock (Kite et al. 2019; Madhusudhan et al. 2020), rendering a surface absent in the traditional sense.

These extreme conditions and processes produce compositional differences between exoplanets that dwarf those between the Solar System terrestrial planets, where from an exoplanet viewpoint the compositional phase space of the Solar System planets is approximately solar (McDonough & Sun 1995; Asplund et al. 2009) except for the volatile budget (Zahnle & Carlson 2020). The delivery and redistribution of volatile compounds during planetary evolution constitutes a major gap in our knowledge, yet is crucial for the origin and evolution of terrestrial atmospheres. The uncertainty in volatile behavior limits both our under-

standing of the planetary environmental context of early Earth and the evolutionary history of rocky exoplanets. Relative to larger, gas or ice-phase dominated worlds, the surface and climatic conditions of rocky planets are sensitive to a variety of physical and chemical processes that operate during their formation, on their precursors bodies, and after their formation. Planetary embryos are anticipated to undergo orbital migration during the disk phase (Bitsch et al. 2019) and iceline positions evolve (Sasselov & Lecar 2000; Owen 2020) during episodic planetesimal formation (Drażkowska & Dullemond 2018), and thus forming planets can sample an evolving mixture of volatiles in various physical and chemical states during accretion (Öberg et al. 2011; Eistrup et al. 2018). Recent work suggests that forming protoplanets and their precursors experience a significant degree of high-energy processing (Sossi et al. 2019; Fegley Jr. et al. 2020; Benedikt et al. 2020) during planetary formation. Planetesimals and protoplanets evolve due to impacts (Quintana et al. 2016; Kegerreis et al. 2020; Denman et al. 2020) and internal radiogenic heating (Lichtenberg et al. 2016, 2019a,b), both of which dramatically alter the thermal budget and volatile content of young rocky worlds. The composition of early- and late-accreted material can alter the initial oxidation state, and thus chemical speciation of the upper mantle and atmosphere (Gaillard & Scaillet 2014; Ortenzi et al. 2020; Zahnle et al. 2020), which is relevant for the planetary environment of prebiotic chemistry (Benner et al. 2019; Rimmer & Rugheimer 2019; Sasselov et al. 2020).

The climatic conditions of young, rocky worlds are therefore established by the extreme cycling of volatiles between planetary reservoirs when the majority of the planet, including its iron core and silicate mantle, is molten. Liquid-gas interactions facilitate rapid chemical equilibration and volatile exchange. The magma ocean phase is thus a crucial evolutionary link between the present state of exoplanets and their formation history (Miller-Ricci et al. 2009; Hamano et al. 2015; Lupu et al. 2014; Schaefer et al. 2016; Bonati et al. 2019). The abundance of water-rich phases in carbonaceous chondritic meteorites and the importance of H₂O as a greenhouse gas motivated pioneering work on steam atmospheres above a magma ocean (Matsui & Abe 1986a,b; Zahnle et al. 1988), which has since been extended to the early thermal and compositional evolution of young protoplanets (Elkins-Tanton 2008, 2011, 2012; Hamano et al. 2013, 2015; Lebrun et al. 2013; Salvador et al. 2017; Marcq et al. 2017; Schaefer et al. 2016; Massol et al. 2016; Tikoo & Elkins-Tanton 2017; Lammer et al. 2018; Katyal et al. 2019; Nikolaou et al. 2019; Bower et al. 2019; Barth et al. 2020; Kite & Barnett 2020). However, meteoritic materials are debris of the specific pathway of the planet formation process in the

Solar System (Wang et al. 2016; Lichtenberg et al. 2018) and may differ substantially from the compositional variety in exoplanetary systems. In addition, the compositional deviations between Solar System chondritic groups result in complex transitions in outgassing behavior (Schaefer & Fegley 2007, 2010), such that the outgassing speciation of chondrite mixtures cannot be deduced from simple superpositions of individual chondrite outgassing speciation (Schaefer & Fegley 2017). Furthermore, the chemical speciation of protoatmospheres is a result of the dynamic and chemical evolution of the silicate mantle during planet solidification, which acts as a reservoir into which major greenhouse gases partition to different degrees during the magma ocean phase. This sequestering into the interior decouples the evolving climate state of the planet from the volatile speciation of its building blocks.

Evidently, we require advanced tools to assess the planetary state shortly after planetary formation to provide the starting point for the long-term climatic and geodynamic evolution, and allow us to explore the range of planetary environments that may form. Aiming to further reduce Solar System-centric assumptions, we here present the evolution and solidification of protoplanets under diverse climatic settings. We focus on major greenhouse gases and compounds that have been suggested to transiently dominate the chemical composition of protoatmospheres. We explore single-species atmospheres composed of H_2 , H_2O , CO_2 , CH_4 , CO , O_2 , and N_2 , since these volatiles can become the dominant absorbers under plausible scenarios of planetary accretion and early evolution. For instance, H_2 can affect the long-term climate due to collision-induced absorption (Pierrehumbert & Gaidos 2011; Koll & Cronin 2019) and its interaction with N_2 has been proposed as a contributor to greenhouse warming on early Earth (Wordsworth & Pierrehumbert 2013a). Furthermore, H_2 is abundant during planet formation and can create transient reducing climates on young planets. Even though H_2O is a trace species in the present-day atmosphere of Earth, it has a strong greenhouse effect which has been routinely discussed in the context of magma ocean protoatmospheres (Matsui & Abe 1986b; Abe & Matsui 1986; Zahnle et al. 1988). The often-remarked influence of H_2O on the tectonic regime of Earth- and super-Earth-sized planets suggest that the near-surface geochemistry is sensitive to its initial abundance (Tikoo & Elkins-Tanton 2017; Schaefer & Elkins-Tanton 2018).

CO_2 is another major greenhouse species typically included in models of coupled magma ocean and atmosphere evolution (Salvador et al. 2017; Bower et al. 2019). However, the major phase and partitioning behavior of carbon during planet formation and magma ocean cooling are poorly constrained (Hirschmann 2012; Dalou et al. 2017;

Fischer et al. 2020) despite their relevance for the climate of rocky planets. For instance, CO_2 can influence the rate of planetary water loss by affecting the cold-trap temperature and the rate of hydrogen escape (Wordsworth & Pierrehumbert 2013b), and may be the major factor that determines the past and present climates of Earth or Mars analogues (Forget & Pierrehumbert 1997; Wordsworth et al. 2017). The dominant species in Earth's present-day atmosphere is N_2 , and but its major biogeochemical cycles remain debated (Wordsworth 2016; Laneuville et al. 2018; Lammer et al. 2018). Specific planetary settings may render CH_4 , CO , and O_2 the major species in planetary atmospheres for transient epochs. For instance, H_2 -dominated atmospheres with a mole fraction of H/C of 0.5 may cool down to a CH_4 -dominated atmosphere at reduced conditions (Hirschmann 2012). CO -dominated atmospheres have been suggested as the result of CO capture from extrasolar debris disks (Kral et al. 2020). Finally, O_2 atmospheres may result from water photolysis and subsequent H_2 loss in steam atmospheres (Luger & Barnes 2015; Schaefer et al. 2016; Wordsworth et al. 2018).

Compositional influences on the radiative balance of protoatmospheres will need to be taken into account to probe and refine the potential orbital transition from Venus-like, primordial runaway greenhouse states, which cool via water dissociation and loss to space, to planets that can cool in an Earth-like fashion by radiating away primordial heat (Hamano et al. 2013). Long-lived magma ocean states may be directly observable with near-future astronomical instrumentation (Lupu et al. 2014; Hamano et al. 2015; Bonati et al. 2019) and link the present-day climates of extrasolar rocky planets with the ancient climate of Hadean Earth. This would allow crucial insights on the thermal and compositional state of young exoplanets and further help constrain the chronology of terrestrial planets in the Solar System (Fegley Jr. et al. 2020). Connecting the thermo-compositional chronology and histories of exoplanets with observations (Schaefer et al. 2016; Wordsworth et al. 2018) is an essential step to bridge astronomy and planetary science. The goal of this work is thus to demonstrate how a sophisticated coupled model of interior and atmosphere interaction can deliver new understanding in how early climate states are derived from the magma ocean epoch of terrestrial planet evolution. We simulate the energetic and compositional evolution of rocky planets from a fully-molten state to their transition to long-term geodynamic and climatic evolution. We describe our coupled numerical framework in Sect. 2 and present results in Sect. 3. We discuss the implications of the work presented here, the main limitations of our approach, and prospects for further studies in Sect. 4, and conclude in Sect. 5.

2. METHODS

In order to simulate the thermal evolution of a magma ocean and its outgassing atmosphere, we couple the interior dynamics code SPIDER (Bower et al. 2018, *Simulating Planetary Interior Dynamics with Extreme Rheology*) to the atmosphere radiative transfer code SOCRATES (Edwards & Slingo 1996, *Suite of Community Radiative Transfer codes based on Edwards and Slingo*). Both codes are stand-alone and are executed and mediated in a serial loop by a python-based framework, which synchronizes initial and boundary conditions between the two codes during runtime (Fig. 1). The major information exchanged between the interior and the atmosphere is the heat flux and surface temperature at the mantle–atmosphere interface, and the distribution of volatile species between the two reservoirs. We subsequently introduce the individual model components and elucidate how information is communicated between them.

2.1. Coupled atmosphere-interior model

2.1.1. Interior

During planetary solidification the rocky planetary mantle undergoes a dynamic transition from a fully molten and turbulent magma ocean to solid-state convection dominated by viscous creep. In order to capture this evolution, SPIDER (Bower et al. 2018, 2019) follows the interior evolution of an initially fully molten planet during cooling and crystallization by solving the energy conservation equation for a spherically symmetric (1-D) mantle that is discretized using the finite volume method:

$$\int_V \rho T \frac{\partial S}{\partial t} dV = - \int_A F_{\text{MO}}^\uparrow \cdot dA + \int_V \rho H dV, \quad (1)$$

with specific entropy S , density ρ , temperature T , directional heat flux F_{MO}^\uparrow , surface area A , internal heat generation per unit mass H , time t , and volume V . The heat flux is determined by four dominant energy transport mechanisms that operate in a semi-molten mantle:

$$F_{\text{MO}}^\uparrow = F_{\text{conv}}^\uparrow + F_{\text{mix}}^\uparrow + F_{\text{cond}}^\uparrow + F_{\text{grav}}^\uparrow, \quad (2)$$

with the directional sum of the individual heat flux contributions from convection F_{conv}^\uparrow , latent heat transport by mixing of melt and solid F_{mix}^\uparrow , conduction F_{cond}^\uparrow , and gravitational separation of melt and solid by permeable flow F_{grav}^\uparrow . Note that the individual and total heat flux contributions in Eq. 2 can be negative, and thus the model can chart the evolution of both cooling planets ($F_{\text{MO}}^\uparrow > 0$) and planets that are heated from the top ($F_{\text{MO}}^\uparrow < 0$) such as the substellar hemisphere of tidally-locked super-Earths that lack an atmosphere. Convection is modeled using mixing length theory by determining a local eddy diffusivity

following Abe (1993, 1995, 1997). Compared to 0-D approaches based on boundary layer theory, mixing length formulations allow for locally-determined variations in temperature and composition at all depths in a planetary mantle. The convective heat flux is

$$F_{\text{conv}}^\uparrow = -\rho T \kappa_h \frac{\partial S}{\partial r}, \quad (3)$$

with eddy diffusivity $\kappa_h \sim u \mathcal{L}_m$, characteristic convective velocity u , and mixing length \mathcal{L}_m . Our nominal model uses a constant mixing length, but we also compute cases where the mixing length is equal to the distance to the nearest mantle interface (i.e., core-mantle boundary or planetary surface) (Stothers & Chin 1997). Energy is also transported due to the displacement of melt and solid by convection, which causes the release and absorption of latent heat:

$$F_{\text{mix}}^\uparrow = -\rho T \Delta S_{\text{fus}} \kappa_h \frac{\partial \phi}{\partial r}, \quad (4)$$

with entropy of fusion $\Delta S_{\text{fus}} = S_{\text{liq}} - S_{\text{sol}}$, liquidus S_{liq} , solidus S_{sol} , and silicate melt fraction ϕ . Conduction is

$$F_{\text{cond}}^\uparrow = -\rho T \kappa_t \left(\frac{\partial S}{\partial r} \right) - \rho c \kappa_t \left(\frac{\partial T}{\partial r} \right)_S, \quad (5)$$

with thermal diffusivity κ_t and adiabatic temperature gradient $(\partial T / \partial r)_S$. Finally, molten rock can separate from its surrounding solid rock matrix by permeable flow, and crystals in liquid-dominated domains can settle or float depending on their density contrast. This exchange of energy is captured by the gravitational separation flux:

$$F_{\text{grav}}^\uparrow = a_g^2 g \rho (\rho_{\text{liq}} - \rho_{\text{sol}}) \zeta_{\text{grav}}(\phi) T \Delta S_{\text{fus}} / \eta_m, \quad (6)$$

with grain size a_g , melt viscosity η_m , density of melt at the liquidus (ρ_{liq}), density of solid at the solidus (ρ_{sol}), and flow mechanism factor $\zeta_{\text{grav}}(\phi)$. $\zeta_{\text{grav}}(\phi)$ parameterizes the flow law as a function of melt fraction, to represent the different regimes from crystal-bearing suspensions at high melt fraction to porous flow at low melt fraction (see Bower et al. 2018).

We assume the silicate mantle to be isochemical, represented by MgSiO_3 . The thermophysical properties of the pure melt and solid phase are parameterized according to Wolf & Bower (2018) and Mosenfelder et al. (2009), respectively. To derive the material properties for the melt-solid aggregate we assume volume additivity when computing the two-phase adiabat. Experiments on synthetic chondritic composition provide the melting curves in the lower mantle (Andrault et al. 2011) and are smoothly joined to the upper mantle melting curves from Hamano et al. (2013), which are based on compiled experimental data on melting of dry peridotite KLB-1 (Takahashi 1986;

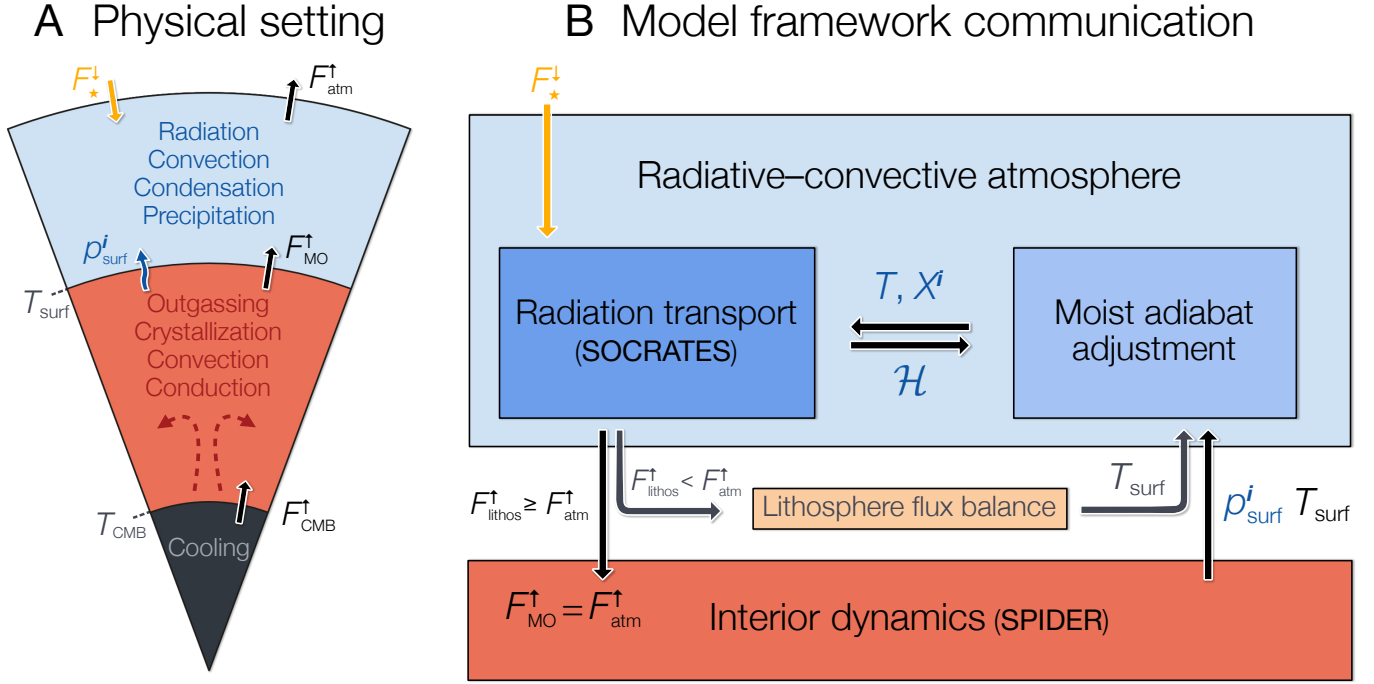


Figure 1. Schematic of the coupled interior–atmosphere model framework. **(A)** Magma ocean domain with dominant processes and nominal direction of energy fluxes. **(B)** Computational model internal communication. Arrow directions show information exchange. Boundary conditions for the interior sub-module are the temperature at the core–mantle boundary T_{CMB} , and the net heat loss to space $F_{\text{MO}}^{\uparrow} = F_{\text{atm}}^{\uparrow}$, which is computed by the atmosphere sub-module. The interior code computes the boundary conditions for the atmosphere: the surface temperature T_{surf} , and the surface partial pressure from volatile outgassing p_{surf}^i . During late-stage cooling, the net heat loss of the planet is controlled by the heat flux in the near-surface (conductive) lithosphere ($F_{\text{lithos}}^{\uparrow}$). In this case, T_{surf} is computed by equilibrating lithospheric and atmospheric heat fluxes. The atmospheric profile is constructed iteratively according to the adiabatic lapse rate and the atmospheric heating rate from radiative transfer. The top-of-atmosphere boundary is the stellar flux at present time and orbit of the planet.

Zhang & Herzberg 1994; Herzberg & Zhang 1996; Zerr et al. 1998; Trønnes & Frost 2002). The melting curves are assumed to be invariant, hence we neglect the potential depression of the solidus by enrichment of volatiles in the residual melt during solidification.

The geophysical (iron) core is not explicitly modelled, but rather a boundary condition is derived at the core–mantle boundary based on energy balance:

$$\frac{dT_{\text{CMB}}}{dt} = -\frac{4\pi r_{\text{CMB}}^2 F_{\text{CMB}}}{m_{\text{core}} c_{\text{core}} \hat{T}_{\text{core}}}, \quad (7)$$

with core mass m_{core} , core heat capacity c_{core} , thermal structure correction factor $\hat{T}_{\text{core}} = T_{\text{core}}/T_{\text{CMB}}$, mass-weighted effective temperature of the core T_{core} , temperature T_{CMB} , radius r_{CMB} , and heat flux F_{CMB} at the core–mantle boundary (CMB). The boundary condition states that the net thermal energy of the core decreases as a consequence of heat removal from the CMB by the silicate magma ocean. This condition does not account for crystallisation of the inner core or heat sources within the core (Chidester et al. 2017). The core is assumed to be isentropic (vigorously convecting), which gives rise to a thermal structure correction factor $\hat{T}_{\text{core}} = 1.147$. Hence for

our initial mantle thermal profile, the initial core temperature $T_{\text{core}} = 5400$ K.

2.1.2. Interior–atmosphere interface

The cooling rate of a mostly molten magma ocean is limited by the ability of the atmosphere to radiate heat to space. Hence during this stage the flux from the interior (upper boundary condition) is $F_{\text{MO}}^{\uparrow} \equiv F_{\text{atm}}^{\uparrow}$, where $F_{\text{atm}}^{\uparrow}$ is computed by the atmosphere sub-module. The surface temperature T_{surf} decreases and the mantle cools, driving a redistribution of volatile species i between the interior and atmosphere through outgassing. Hence a new surface temperature and distribution of volatiles in the atmosphere is derived, which are then used to update the thermal boundary condition and atmospheric composition of the atmosphere sub-module. During the later stages of crystallization, a stiff viscous lid forms once the surface temperature drops below the rheological lockup point such that the interior heat flux can decrease below values that can theoretically be sustained by the atmosphere. Cooling of the interior to space is then inhibited due to the comparatively slow rate of energy transfer through the conductive lid (lithosphere), rather than blanketing by the atmosphere.

Molecule	α (ppmw/Pa)	β (non-dim.)
H ₂ O	1.033×10^0	1.747
H ₂	2.572×10^{-6}	1.000
CO ₂	1.937×10^{-9}	0.714
CH ₄	9.937×10^{-8}	1.000
N ₂ ⁻	$7.416 \times 10^{+1}$	4.582
N ₂	7.000×10^{-5}	1.800
CO	1.600×10^{-7}	1.000
O ₂	–	–

Table 1. Partitioning data and Henry coefficient fit parameters as shown in Fig. 2. Data references – H₂O: Silver et al. (1990); Holtz et al. (1995); Moore & Carmichael (1998); Yamashita (1999); Gardner et al. (1999); Liu et al. (2005); H₂: Gailard et al. (2003); Hirschmann et al. (2012); CO₂: Mysen et al. (1975); Stolper & Holloway (1988); Pan et al. (1991); Blank et al. (1993); Dixon et al. (1995); CH₄: Ardia et al. (2013); Keppler & Golabek (2019); N₂: Libourel et al. (2003); Li et al. (2013); Dalou et al. (2017); Mosenfelder et al. (2019); CO: fit constants from Yoshioka et al. (2019); O₂: see main text. N₂⁻ indicates the partition coefficients for nitrogen species under reduced conditions with a redox state below the iron-wüstite buffer (IW), $fO_2 \lesssim IW$.

To account for this we decouple the temperature profile of the lithosphere from the internal profile that is spatially resolved by SPIDER. The surface temperature is then updated by solving for conductive transport in a shallow surface region,

$$\mu_1 \frac{dT_{\text{surf}}}{dt} = F_{\text{atm}}^{\uparrow} - F_{\text{lithos}}^{\uparrow} \leq \epsilon, \quad (8)$$

with the heat capacity of the near-surface layer μ_1 , the lithosphere heat flux $F_{\text{lithos}}^{\uparrow}$ computed from the energy gradient near the surface using SPIDER, and convergence factor $\epsilon = 1 \text{ W m}^{-2}$. The atmosphere is then evolved until it equilibrates with the interior heat flux (Fig. 1). When a boundary skin is considered (Fig. 9, iv), we account for the ultra-thin thermal boundary layer at the surface that offsets the surface temperature from the mantle potential temperature by several hundred Kelvin. The relationship between the boundary layer temperature drop and the surface temperature is derived by equating the heat flux in an ultra-thin (numerically unresolved) viscous boundary layer with radiation at the surface. For surface temperatures between 1400 K and 2000 K, we then *a priori* solve for the thermal boundary layer structure at steady-state using the heat flux balance and representative material properties of the melt. This determines that the boundary layer temperature drop scales with the surface temperature cubed with a constant of proportionality of 10^{-7} K^{-2} (Bower et al. 2018, Eq. 18).

A solubility law relates the abundance of a volatile i in the interior (in melt) to its abundance in the atmosphere, according to the partial pressure of the volatile at the sur-

face:

$$p_{\text{surf}}^i = \left(\frac{X_{\text{magma}}^i}{\alpha_i} \right)^{\beta_i}, \quad (9)$$

with the surface partial pressure p_{surf}^i , abundance in the melt X_{magma}^i , and Henrian fit coefficients α_i and β_i of species i from petrologic data (Tab. 1, Fig. 2). In this compilation we introduce two different relations for nitrogen to illustrate its strongly diverging solubility behaviour above and below the iron-wüstite buffer (Libourel et al. 2003). The chemical composition (as quantified by its redox state, fO_2) of the magma ocean controls the speciation of outgassed volatiles (Sossi & Fegley 2018, e.g.). These chosen relations hence serve to illustrate the solubility behaviour for a mantle composition that allows the stability of given volatile species.

The partial pressure of a volatile p_{surf}^i then relates to the mass of the volatile in the atmosphere (Bower et al. 2019):

$$m_i^g = 4\pi R_p^2 \left(\frac{\mu_i}{\bar{\mu}_{\text{atm}}} \right) \frac{p_{\text{surf}}^i}{g}, \quad (10)$$

with planetary radius at the interior–atmosphere interface R_p , molar mass μ_i of species i , mean atmospheric molar mass $\bar{\mu}_{\text{atm}}$, and gravity g . We assume O₂ to be insoluble and thus its atmospheric mass is constant with time. Our treatment of degassing assumes the respective volatile to be in solution equilibrium between the magma ocean and the overlying atmosphere. If outgassing from the magma ocean would be governed by bubble nucleation instead, the degassing rate may decrease (Hamano et al. 2013; Ikoma et al. 2018, cf.).

2.1.3. Atmosphere

The atmosphere sub-module of the coupled framework establishes the atmospheric thermal and compositional profile, based on the surface partial pressures p_{surf}^i of the volatile species i and surface temperature T_{surf} . In the earliest, hottest phase, the atmospheric profile follows a dry adiabat, but with cooling the upper atmosphere saturates, condenses, and follows the saturation vapor curve (Pierrehumbert 2010). Because the net energy flux to space depends on the radiating layer within the atmosphere, it is important to consider the influence of the change in atmospheric lapse rate when temperatures are cool enough for condensation to occur. We use a fourth-order Runge-Kutta integrator to compute the atmosphere lapse rate by integrating upwards from the planetary surface where $T = T_{\text{surf}}$:

$$\frac{d \ln T}{d \ln P} = R/c_{p,i}(T) \text{ if unsaturated} \quad (11)$$

$$= RT/L_i \text{ if saturated,} \quad (12)$$

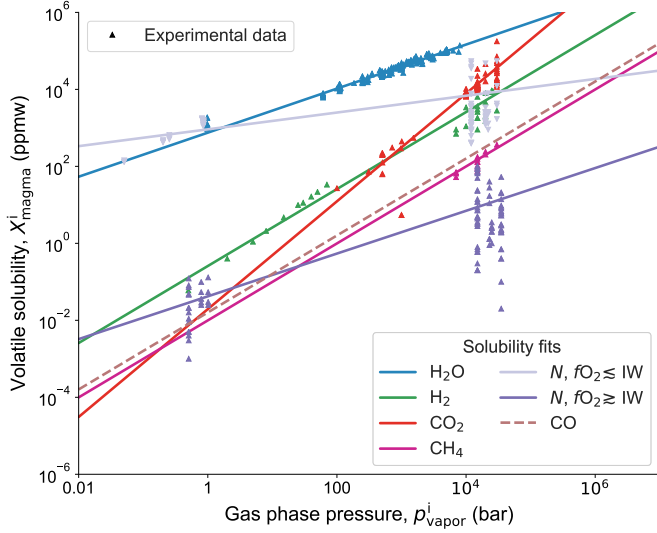


Figure 2. Relationship between ambient pressure and solubility in silicate melts for the considered volatiles from petrological experiments. Data references and fit coefficients α_i and β_i are given in Tab. 1. Nitrogen solubility is independently calculated where the oxygen fugacity (fO_2) of the magma is below or above the iron-wüstite buffer (IW), respectively.

with universal gas constant $R = 8.314 \text{ J K}^{-1} \text{ mol}^{-1}$, ambient temperature T , and specific heat capacity $c_{p,i}$ and latent heat L_i per individual species i . We treat all gases as ideal to determine thermodynamic properties, such as their critical points and latent heats (Pierrehumbert 2010). Heat capacities are temperature-dependent:

$$c_{p,i}(\hat{T}) = A_i + B_i\hat{T} + C_i\hat{T}^2 + D_i\hat{T}^3 + E_i/\hat{T}^2, \quad (13)$$

with $\hat{T} = T(K)/1000$, and the fit constants A_i – E_i provided in the NIST Chemistry WebBook, SRD 69 (Cox et al. 1984; Chase Jr 1998). When condensation occurs during upward integration along the adiabat (Eq. 12), a fraction of the gas phase is converted to a condensate phase according to the saturation vapor curve p_{sat}^i of the respective species and removed from the gas parcel (Pierrehumbert 2010). In the coupled framework, this may occur at ground level indicating formation of an ocean (or glacier) (Marcq et al. 2017). The formulation follows a dry adiabat in the lower troposphere, and a moist convective profile once the dry adiabat intersects the Clausius-Clapeyron slope where condensation occurs. The behavior of the adiabat structure is illustrated in Fig. 3 for H_2 , H_2O , CO_2 , CH_4 , CO , O_2 , and N_2 , with surface pressure $P_{\text{surf}} = 260 \text{ bar}$, surface temperature $T_{\text{surf}} = 1000 \text{ K}$, and top-of-atmosphere (TOA) pressure of $10^{-5} \text{ bar} = 1 \text{ Pa}$.

To account for a potential stratosphere, we iterate between the adiabat adjustment and radiation atmosphere sub-modules by computing the atmospheric heating rate \mathcal{H} (see below). We set the atmosphere to isothermal

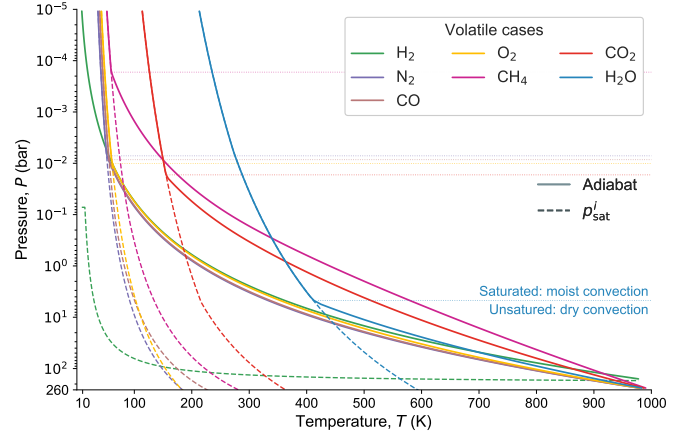


Figure 3. Thermal structure for single species atmospheres with fixed surface pressure equivalent $P_{\text{surf}} = 260 \text{ bar}$ and surface temperature $T_{\text{surf}} = 1000 \text{ K}$. In the lower troposphere the atmospheric structure aligns with the dry adiabat until it intersects with the species-dependent saturation vapor curve, p_{sat}^i , at which point condensates form and the lapse rate follows a moist convective profile (Eqs. 11 and 12).

above the tropopause (Schaefer et al. 2016) and recompute the radiation balance using this adjusted T – P profile. This procedure yields an approximation to the tropopause location and stratospheric temperature structure and is computationally efficient compared to a time-stepped radiative equilibrium calculation. To compute the heat flux to space depending on composition and thermal profile of the atmosphere, we utilize the SOCRATES radiative transfer suite (Edwards & Slingo 1996; Sun 2011). SOCRATES is incorporated in the UK Met Office Unified Model (Amundsen et al. 2014, 2016) and ROCKE-3D (Way et al. 2017), and solves the plane-parallel, two-stream approximated radiative transfer equation, which we employ in the limit without scattering. The thermal flux is

$$\pm \frac{1}{D} \frac{dF_{\text{th}}^{\uparrow\downarrow}}{d\tau} = F_{\text{th}}^{\uparrow\downarrow} - \pi B(T), \quad (14)$$

with thermal upward and downward fluxes, F_{th}^{\uparrow} and $F_{\text{th}}^{\downarrow}$ respectively, optical depth τ , Planck intensity $B(T)$, temperature T , and diffusivity factor $D = 1.66$. Note that F , τ , and B are dependent on wavenumber $\tilde{\nu}$, which we omit here for clarity of notation. The incident stellar radiation is expressed as the direct, unscattered component,

$$F_{\star}^{\downarrow} = F_{\star,\text{TOA}} \cdot e^{-\tau/\mu}/\mu, \quad (15)$$

with $\mu = |\cos \theta|$ and mean stellar zenith angle $\theta = 54.55^\circ$, as a compromise between a daytime-averaged and insolation-weighted choice (Cronin 2014). The surface-averaged stellar flux at the top of the atmosphere (TOA) is calculated as

$$F_{\star,\text{TOA}}(\tau_{\star}) = \frac{1 - \alpha_p}{4} \frac{\mathcal{L}_{\star}(\tau_{\star})}{4\pi a_p^2}, \quad (16)$$

with planetary albedo, bolometric luminosity of the star \mathcal{L}_* , and mean orbital distance of the planet a_p . τ_* indicates the time since star formation. We assume a constant planetary albedo $\alpha_p = 0.2$, which reasonably approximates the albedo over a wide temperature interval of steam atmospheres (Hamano et al. 2015). Varying albedo due to scattering or cloud effects can influence the heat budget of the cooling planet (Pluriel et al. 2019). For the time evolution of the stellar luminosity \mathcal{L}_* we employ a bilinear interpolation in the mass-time $[M_*, \tau_*]$ plane of the stellar evolution models of Baraffe et al. (1998, 2015) and Girardi et al. (2000). Since we exclusively focus on Sun-like stars, we use the Solar spectrum from Kurucz (1995). The total upward and downward fluxes are the sum of the thermal and stellar components,

$$F_{\text{net}}^{\uparrow\downarrow} = F_{\text{th}}^{\uparrow\downarrow} + F_{\star}^{\uparrow\downarrow} \quad (17)$$

and thus the total atmospheric heat flux of the planet, which is required for the upper boundary condition of the interior, is

$$F_{\text{MO}}^{\uparrow} \equiv F_{\text{atm}}^{\uparrow} = F_{\text{net}}^{\uparrow} - F_{\text{net}}^{\downarrow}. \quad (18)$$

The optical depth at a particular wavenumber in differential form is

$$\begin{aligned} d\tau &= -k(z)dz = -k_{\rho}(z)\rho(z)dz \\ &= -\sum \zeta_i(z)k_{\rho}^i(z)\rho(z)dz, \end{aligned} \quad (19)$$

with mass mixing ratio ζ_i and mass absorption coefficient k_{ρ}^i for volatile species i , height z , total mass absorption coefficient $k_{\rho}(z)$, and total absorption coefficient $k(z) = k_{\rho}(z)\rho(z)$. The heating rate is then

$$\mathcal{H} = -\frac{dF}{dz} = \frac{g\bar{\mu}_{\text{atm}}P}{RT} \frac{dF_{\text{atm}}}{dP}, \quad (20)$$

with gravitational acceleration g and mean molecular weight $\bar{\mu}_{\text{atm}}$. SOCRATES achieves computational efficiency by employing the correlated- k method to solve the transmission function: absorption coefficients with similar values are grouped and summed over the atmospheric layers with different weights. k -coefficients are calculated using a combination of correlated- k (Goody et al. 1989) and the exponential sum fitting of transmissions (Wiscombe & Evans 1977). Line-by-line opacity data is banded into n_k subintervals and an average absorption coefficient is calculated from the top of the atmosphere to an optical depth of one,

$$\begin{aligned} k_{\rho, \text{avg}}^i(\tilde{\nu})u_{\tau=1}^i &= \int_{z_z=1}^{\infty} dz' \zeta_i(z') \rho(z') k_{\rho}^i(\tilde{\nu}, z') \\ &= \frac{1}{g} \int_{P_{\tau=1}}^{P'} dP' \zeta_i(P') k_{\rho}^i(\nu, P') \equiv 1(21) \end{aligned}$$

with column density $u_{\tau=1}^i$ from the top of the atmosphere to $\tau = 1$ for species i . For each subinterval l the weighted transmission from line-by-line coefficients is fitted to the transmission function, such that

$$\int_{g_l}^{g_{l+1}} dg w(g) e^{k_{\rho}(g)u_j} \approx e^{k_{\rho, \text{opt}}^l u_j} \quad (22)$$

with transmission $e^{k_{\rho, \text{opt}}^l u_j}$ for a set of n_u column densities, u_j , weighting function w , and optimal k -coefficient $k_{\rho, \text{opt}}^l$ in the given subinterval l . Here, we use differential Planckian weights w_l at transmission temperature normalized per band,

$$\int_0^1 dg w(g) = \sum_{l=1}^{n_k} w_l = 1. \quad (23)$$

The total flux per wavenumber band b is then

$$F_b = \sum_{l=1}^{n_k} w_l^{\tau=1} F_l, \quad (24)$$

with weights $w_l^{\tau=1}$, where the optical depth $\tau = 1$ (Amundsen et al. 2014), and flux F_l per subinterval. We use a band structure that covers the wavenumber range from 1–30000 cm^{-1} and consists of 318 individual bands with a spacing of $\Delta\nu_{1-120} = 25 \text{ cm}^{-1}$ from 1–3000 cm^{-1} , $\Delta\nu_{121-280} = 50 \text{ cm}^{-1}$ from 3000–11000 cm^{-1} , and $\Delta\nu_{281-318} = 500 \text{ cm}^{-1}$ from 11000–30000 cm^{-1} . We tabulate the k -coefficients on a P, T grid of 21 pressures, $P \in [10^{-11}, 10^{-8}, 10^{-6}, 10^{-5}, 10^{-4}, 5 \times 10^{-4}, 10^{-3}, 5 \times 10^{-3}, 10^{-2}, 5 \times 10^{-2}, 10^{-1}, 5 \times 10^{-1}, 10^0, 5 \times 10^0, 10^{+1}, 5 \times 10^{+1}, 10^{+2}, 5 \times 10^{+2}, 10^{+3}, 5 \times 10^{+3}, 10^{+4}]$ bar, and 15 temperatures, $T \in [100, 250, 400, 600, 800, 1000, 1250, 1500, 1750, 2000, 2333, 2666, 3000, 3500, 4000]$ K. The opacity data that is used as input to generate the k tables is referenced in Tab. A1.

3. RESULTS

We explore the energetic feedback between a solidifying magma ocean and its outgassed atmosphere. By focusing on single species atmospheres consisting of either H_2 , H_2O , CO_2 , CH_4 , CO , O_2 , or N_2 , we can isolate the influence of radiative properties and partitioning behavior on planetary cooling timescales. As a baseline for comparing the thermal chronologies of the coupled magma ocean–atmosphere systems, we choose the initial volatile abundance to produce an outgassed atmosphere of 260 bar after mantle solidification. We ignore trapped volatiles in the solidified rock since this abundance is negligible compared to volatile partitioning into the melt. For the case of H_2O , 260 bar roughly corresponds to a steam atmosphere equivalent of one Earth ocean. All models begin with a fully molten planetary mantle at 100 Myr after star formation.

3.1. Steady-state atmospheric radiation balance

Before proceeding to evaluate the evolution of the coupled mantle-atmosphere system during magma ocean solidification, we illustrate the heat flux properties of the radiative-convective atmosphere model. We first discuss the steady-state behavior in order to validate our atmospheric model with previous approaches and illustrate key physical mechanisms that control the heat loss to space. In Fig. 4A we compare the outgoing thermal radiation (F_{th}^{\uparrow}) for all volatiles for surface pressures of 260 bar and 1 bar, which capture the instantaneous state of the atmosphere near the end and start of outgassing, respectively. For the H₂O–260 bar case we recover the tropospheric radiation limit (Simpson 1929; Nakajima et al. 1992), with a near-constant F_{th}^{\uparrow} of 282.5 W m⁻² in the window from ≈ 300 –2000 K surface temperature. Our computed radiation limit closely aligns with recent estimates from Goldblatt et al. (2013), Kopparapu et al. (2013), and Hamano et al. (2015) until about 2000 K, and further compares favorably to 280 W m⁻² in Marcq et al. (2017) and 282 W m⁻² in Katyal et al. (2019). For 260 bar, H₂ shows a strong depression in the outgoing radiation below the H₂O radiation limit for $T_{\text{surf}} \lesssim 1700$ K which appears to be due to its strongly pressure-dependent opacity. However, validation of the opacity trend at the low temperature range near the surface where H₂ has high density requires a non-ideal H₂ equation of state. At the lower pressure of 1 bar the radiation limit for H₂O ranges from $T_{\text{surf}} \approx 300$ –700 K and the outgoing radiation for H₂ is below H₂O for $T_{\text{surf}} \lesssim 450$ K. CO₂ and CH₄ have similar F_{th}^{\uparrow} from ≈ 500 K and higher, which is intermediate compared to the lowest F_{th}^{\uparrow} (H₂) and the highest F_{th}^{\uparrow} (O₂). Relative to the other volatiles, N₂, CO, and O₂ do not significantly restrict the heat flux to space. None of the volatiles show strong depression in the outgoing radiation at 1 bar and high temperature.

Fig. 4B displays the net outgoing flux ($F_{\text{atm}}^{\uparrow} \equiv F_{\text{MO}}^{\uparrow}$, Eq. 18), which serves as the boundary condition at the interior–atmosphere interface when the surface is mostly molten. A significant feature of the 1.0 au cases is the extended radiation limits for H₂O between $T_{\text{surf}} \approx 300$ –1000 K and for H₂ for $T_{\text{surf}} \lesssim 750$ K. Once planets are cool enough, their atmospheres become optically thick, and the outgoing radiation becomes smaller than the incoming stellar radiation. This transition occurs below 300 K except for H₂, so planets at 1.0 au with 10 bar H₂ atmospheres cannot cool down below ≈ 750 K in the absence of other processes, such as escape. For closer-in planets at 0.4 au, the transition points from the cooling to the heating regimes for the various volatiles are separated over a larger range of surface temperature than for planets at 1 au. CO₂ and CH₄ show net flux depressions at $T_{\text{surf}} \lesssim 500$ K, and CO₂ and CH₄ at $T_{\text{surf}} \lesssim 300$ K. The steady-

state calculations reveal the influence of the planetary orbit and atmospheric composition on planetary heat loss, but they do not consider the time variations in both atmospheric volatile budget and thermal state due to progressive solidification of the mantle. The calculations suggest that all volatiles with significant flux depression (H₂O, H₂, CO₂, and CH₄) may experience a feedback between outgassing and solidification, resulting in marked differences in the cooling timescales. The timescales and atmospheric budgets, however, depend additionally on the solubility of the volatile in the melt. In the next section we thus consider the time-dependent feedbacks between the interior and atmosphere during the early evolution of planets starting from a fully-molten magma ocean.

3.2. Time evolution of the coupled magma ocean–atmosphere

Fig. 5 displays the evolution of a solidifying magma ocean for an atmosphere dominated by either H₂, H₂O, CO₂, CH₄, CO, O₂, or N₂ for an Earth-sized planet at 1.0 au from a Sun-like star after 100 Myr after star formation. Simulations terminate when the planet reaches a global melt fraction of $\phi_{\text{mantle}} \leq 0.5$ wt.%. The cooling sequence can be classified into three principal episodes, which vary in duration depending on the volatile species. The first phase is dominated by a fully molten magma ocean ($\phi_{\text{mantle}} \approx 1$) and varies from $\approx 10^2$ yr (CO, O₂, and N₂) to $\approx 10^3$ yr (H₂O, CO₂, CH₄), and $\approx 10^4$ yr (H₂) in duration. The interior temperatures are superliquidus and the interior convects vigorously which maintains a high surface temperature. During this phase, heat flux, surface temperature, and outgassing of volatiles to the atmosphere vary only minimally. Once the mantle starts to crystallize, the surface temperature decreases faster than during the fully molten phase because heat is not delivered as efficiently to the surface from the deep interior. This is because heat transport is diminished in mixed solid–liquid aggregates or fully solid rock relative to molten magma due to larger viscosity. The second phase occurs when the magma ocean is solidifying from the core–mantle boundary to the surface. This phase lasts until $\approx 10^3$ yr for CO, O₂, N₂, and $\approx 10^4$ yr for H₂O, CO₂, CH₄, and $\approx 10^6$ yr for H₂. Subsequently the rheological front, which is defined as the (quite abrupt) increase in viscosity from a melt- to solid-dominated aggregate ($\phi \approx 0.4$), reaches the surface. This signals a transition to sluggish convection in the interior and hence a protracted cooling phase (phase 3). Solidification proceeds until the mantle reaches near-zero melt fraction, which takes ≈ 1 Myr for all volatiles but H₂. The H₂ planet case does not solidify within 100 Myr simulation runtime.

The heat flux, surface temperature, and mantle fraction (Fig. 5A, B, and C) result from the feedback between man-

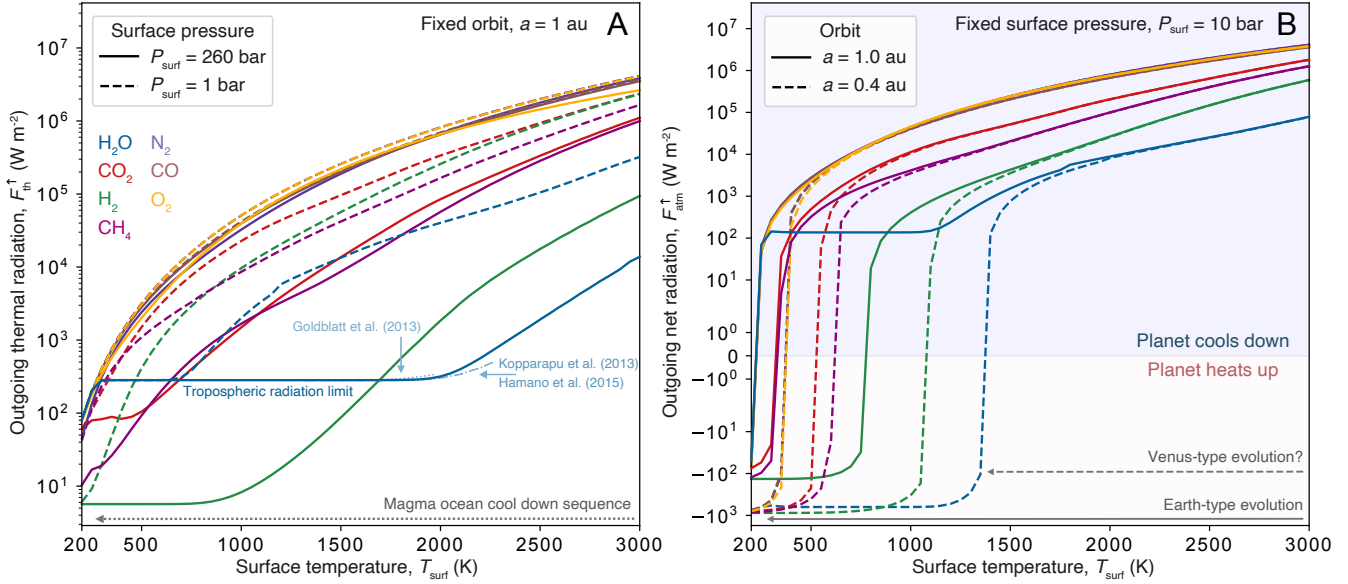


Figure 4. Outgoing radiation for single-species atmospheres and varying planetary settings. **(A)** Outgoing thermal radiation as a function of surface temperature for planetary orbital distance $a = 1$ au, and surface pressure equivalent of $P_{surf} = 260$ bar or 1 bar. **(B)** Outgoing net radiation (thermal minus instellation, Eqs. 17 and 18) as a function of surface temperature for $a = 1.0$ au or $a = 0.4$ au, with fixed surface pressure of $P_{surf} = 10$ bar and star age $\tau_* = 100$ Myr. For closer-in planets with fixed atmospheric content the incoming stellar radiation exceeds the heat flux to space and they enter the heating regime. The shown results are computed with a fixed planetary albedo of $\alpha_P = 0.2$.

tle solidification and thermal blanketing by the atmosphere, which limits the heat flux to space depending on the atmospheric conditions. Fig. 5D, E, F show the outgassing sequence that defines the surface pressure, and total atmospheric and interior volatile mass fraction. The outgassing sequences differ substantially between cases due to the different solubilities of the volatiles in melt (Fig. 2). Generally, H_2O and N_2 are the most soluble in magma and hence they outgas late relative to other cases. H_2O does not outgas completely to establish a 260 bar atmosphere because its solubility is high enough to trap a fraction of H_2O in the remaining ≈ 0.5 wt.% of melt. O_2 is treated as insoluble, and hence its atmospheric mass and surface pressure is constant. For all other cases, outgassing is effectively driven by the reduction in mantle melt fraction, hence outgassing mostly occurs during phase 2 when solidification begins until the rheological front reaches to the surface (at which time ≈ 70 – 80 wt.% of the planetary mantle is solidified). Outgassing then proceeds until all the volatile mass is transferred to the atmosphere from the interior. Even though volatiles such as H_2O can be stored in nominally anhydrous minerals, their abundance in the deep mantle is typically around ~ 0.1 wt.% (Peslier et al. 2018) which is negligible in comparison to the atmospheric reservoir.

To illustrate the combined evolution of the planet's interior and atmosphere we show each case at two distinct times in Fig. 6. This plot shows the pressure–temperature

structure of the atmosphere due to both its composition and radiative-convective structure. H_2 displays the most pronounced vertical stratification because of its low molecular weight and slow cooling, followed by CH_4 , H_2O , CO_2 , then CO , N_2 , and CO . However, at 1 Myr the H_2O case shows departure of its vertical structure relative to the earlier time and the CH_4 and CO_2 cases, and its surface temperature is closer to the ones of CO , O_2 , and N_2 . This emphasizes the influence of the coupled thermal evolution of the atmosphere on the overall planetary structure. Fig. 5B reveals the distinct evolution when comparing H_2O with the CH_4 and CO_2 cases. The surface temperature for the H_2O case is near-constant between 10^4 – 10^6 yr. However, once the heat flux from the interior drops significantly the surface temperature falls rapidly (Fig. 5A) and the atmosphere collapses. This is because for intermediate surface temperatures the atmospheric heat flux remains constant since the upper atmosphere aligns with the H_2O moist adiabat, i.e., the heat flux is regulated by the radiation limit (Figs. 3 and 4). Hence, when the internal heat flux cannot sustain heat loss above the radiation limit anymore, the lithosphere cools rapidly until equilibrium between the internal and atmospheric heat fluxes is reached. Because of the high solubility of H_2O , most H_2O outgasses after $\gtrsim 90$ wt.% of the mantle is already solidified and the surface temperature favors condensation. Hence outgassed water immediately forms a condensed surface water reservoir rather than contributing to the atmospheric greenhouse ef-

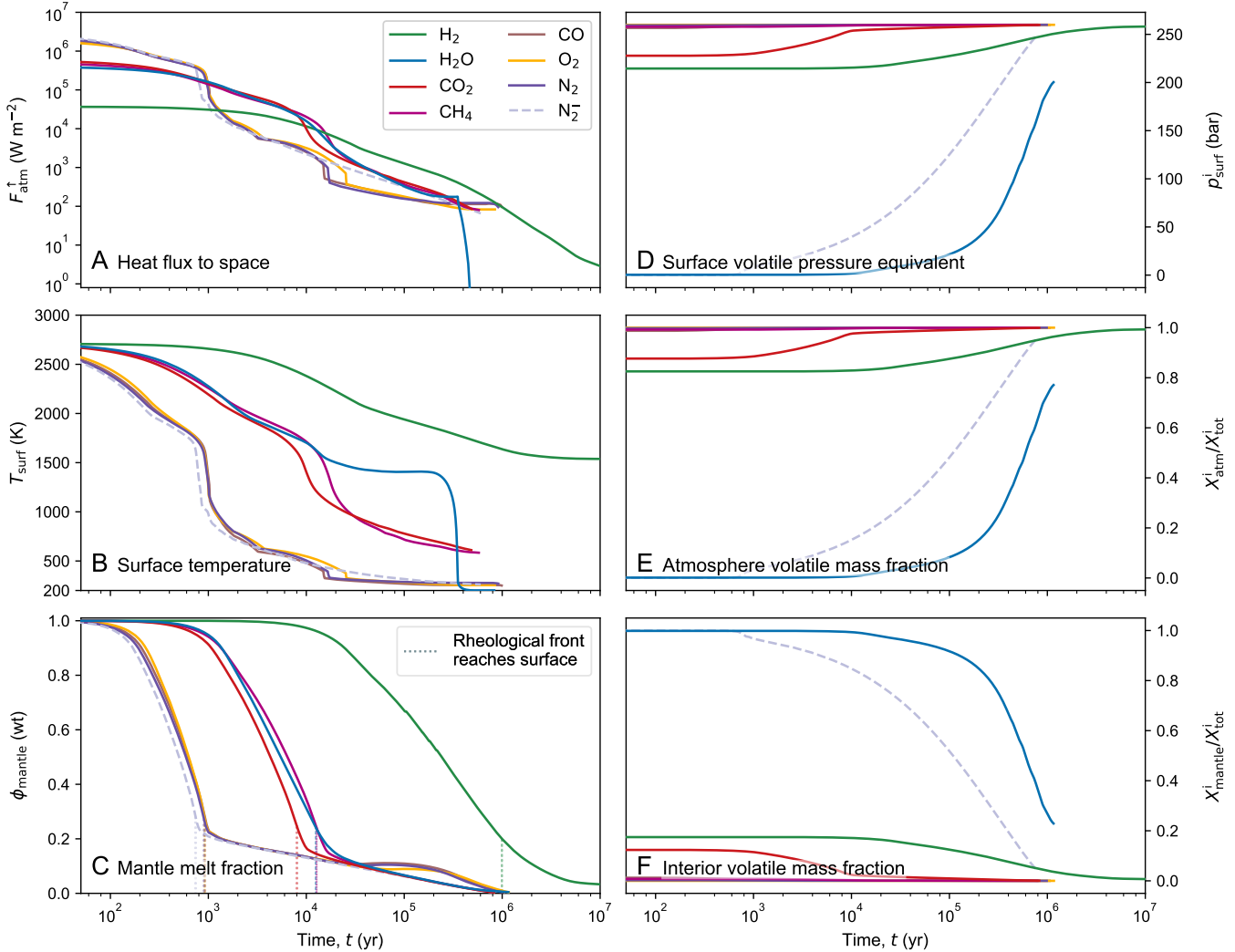


Figure 5. Coupled evolution of mantle and atmosphere. N₂ is considered for an oxidized (N₂) and reduced (N₂⁻) case. Evolution can be classified into three groups of similar behavior: (i) H₂, with the most protracted solidification chronology, (ii) H₂O, CO₂, and CH₄ with intermediate cooling time, and (iii) CO, O₂, and N₂/N₂⁻ with the shortest cooling time. Times shown are relative to model start, i.e., 100 Myr shifted to star formation. See main text for a more extensive description.

fect. CO₂ and CH₄ on the other hand are less effective as absorbers and the planet can cool faster until ≈ 1 Myr after model start. These volatiles, however, are significantly less soluble in magma compared to H₂O, and do not facilitate a condensation-induced radiation limit for temperatures relevant to magma ocean cooling (Fig. 4). Therefore, the corresponding planets steadily cool down and their atmospheres grow to their full outgassed 260 bar surface pressure early during magma ocean evolution.

3.3. Observational links between atmospheric and interior state

The sequence of planet solidification for the different volatiles produces time-evolving atmospheres with different thermal states and spatial extents, which furthermore can provide predictions on the observable spectral signa-

ture of the atmosphere. For single-species atmospheres, the top-of-atmosphere emission spectra show distinct features during their evolution and are distinguishable from one another. Fig. 7 displays the planetary spectra at three distinct times during evolution when the rheological transition reaches the mantle–atmosphere interface for the different volatile groups at $t = 10^3$, 10^4 , and 10^6 yr (Fig. 5). The rheological transition denotes when the mode of heat transfer in the mantle transitions from vigorous convection and rapid cooling to more protracted cooling that is dominated by solid-state convection. In general, higher wavenumber features are muted as the planet solidifies and the spectra across the different absorbers reveal distinct features from each other. H₂ during early times is dominated by the wavenumber regions around $\nu \approx 20000$ cm⁻¹ but at 1 Myr these regions do not contribute sig-

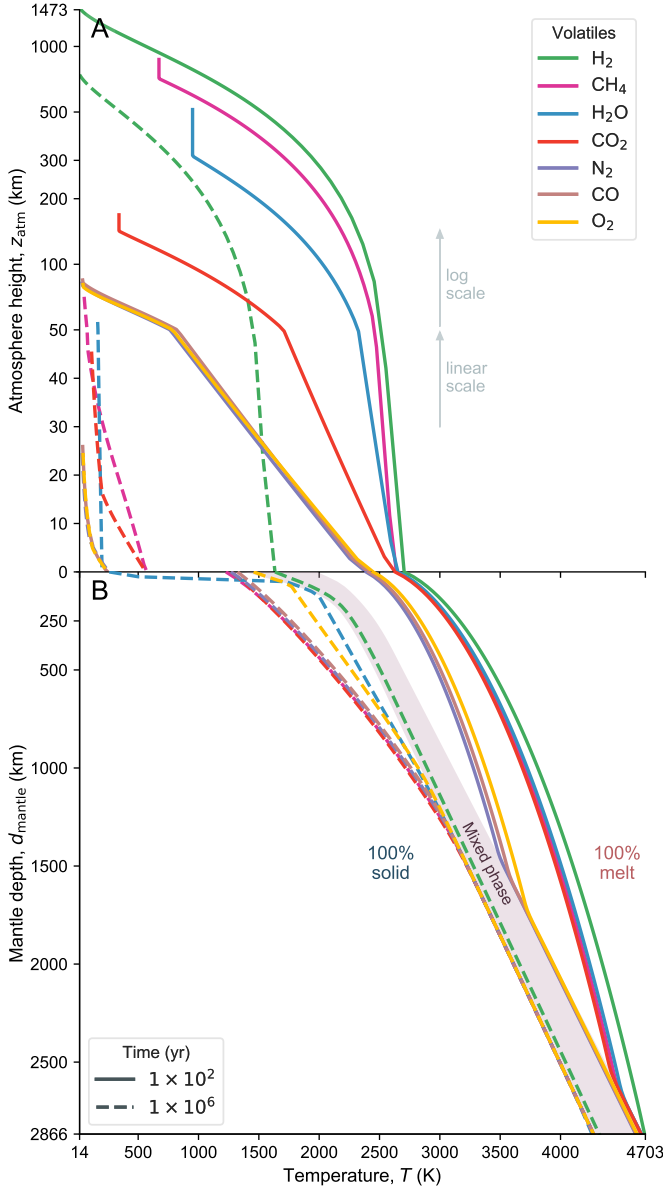


Figure 6. Thermal and vertical structure of the atmosphere and interior at two snapshots during evolution. **(A)** Atmospheric height stratification. Early atmospheres are thermally expanded and lower molecular weight atmospheres extend to great height. Note the transition in the height axis between linear and log scale at 50 km. **(B)** Interior evolution. The transition region from fully-molten to fully-solidified rock is illustrated with a gray background (‘Mixed phase’). Right of this area heat transfer is very rapid and dominated by vigorous convection in the liquid magma, left of it heat transfer is much slower and dominated by solid-state creep processes.

nificantly to the heat flux anymore and the planet is dominantly cooling through the regions around $\nu \lesssim 3000 \text{ cm}^{-1}$. Similar trends occur for H_2O , CO_2 , and CH_4 . H_2O evolves in regions of $4000\text{--}6000 \text{ cm}^{-1}$, CO_2 in several distinct regions from $\approx 4000\text{--}15000 \text{ cm}^{-1}$, and CH_4 at $\approx 3000 \text{ cm}^{-1}$

and between $\approx 9000\text{--}11000 \text{ cm}^{-1}$. CO , N_2 , and O_2 cool very rapidly and their absorbing regions are confined to ranges around $\approx 1500 \text{ cm}^{-1}$ for O_2 , $\approx 2000 \text{ cm}^{-1}$ and $\approx 4100 \text{ cm}^{-1}$ for CO , and $\approx 2500 \text{ cm}^{-1}$ and $\approx 4500 \text{ cm}^{-1}$ for N_2 . In summary, H_2 , H_2O , CO_2 , and CH_4 display the strongest departures from the blackbody curve, which means they absorb more longwave radiation that is emitted from the planetary surface. O_2 , CO , and N_2 bear significant resemblance to the blackbody curve, so alter the radiation properties of the planet to a lesser degree. Nevertheless, N_2 displays absorption features around ≈ 2500 and $\approx 4700 \text{ cm}^{-1}$ during the fully-molten phase.

Astronomical observations are typically only possible at confined wavelength regions and thus it is necessary to connect magma oceans with outgassed atmospheres of different compositions to specific features at certain wavelengths. Therefore, Fig. 8 compares the contribution of different atmospheric layers to the outgoing flux for the total and wavelength-specific flux. We quantify the normalized fraction of outgoing net flux that escapes to space from a particular layer j in the atmosphere (Drummond et al. 2018):

$$\mathcal{CF}_F = \frac{2\pi B(\tau_{j,j+1})}{D} (e^{-D\tau_j} - e^{-D\tau_{j+1}}). \quad (25)$$

Fig. 8A illustrates the contribution of the top-of-atmosphere net outgoing flux from different atmospheric layers at different times, and visualizes the dominant photospheres of the magma ocean planets at the transition from melt- to solid-dominated. The flux for the CO , N_2 , and O_2 cases is dominated by near-surface layers since these volatiles are least effective as absorbers. In particular for the N_2 case, the magma ocean surface itself is the dominant emitter, suggesting that planets with N_2 atmospheres may enable their magma ocean surface to be probed directly. Depending on atmospheric conditions (pressure–temperature), the photosphere shifts to different levels and can sometimes be vertically split, i.e., emission can be dominated by two or multiple distinct regions. For instance, the H_2 case displays two local maxima of the contribution function at $\approx 8 \times 10^{-3}$ and ≈ 1 normalized pressure. The \mathcal{CF}_F -weighted pressure level (the *photosphere* of the planet) lies approximately between these two maxima. The large scale height in Fig. 6 suggests that SOCRATES overestimates the opacity of the upper of the two maxima since the height variation of gravity $g(z)$ is not considered. This could affect the cooling rate by underestimating the mass path, $dm \sim dp/g$. For a related discussion for water worlds see Arnscheidt et al. (2019). Therefore, further work is required to estimate the cooling behavior of extended H_2 atmospheres. The H_2O and CO_2 cases mostly emit from intermediate pressure levels between $\approx 1 \times 10^{-1}$ and $\approx 5 \times 10^{-3}$ normalized pres-

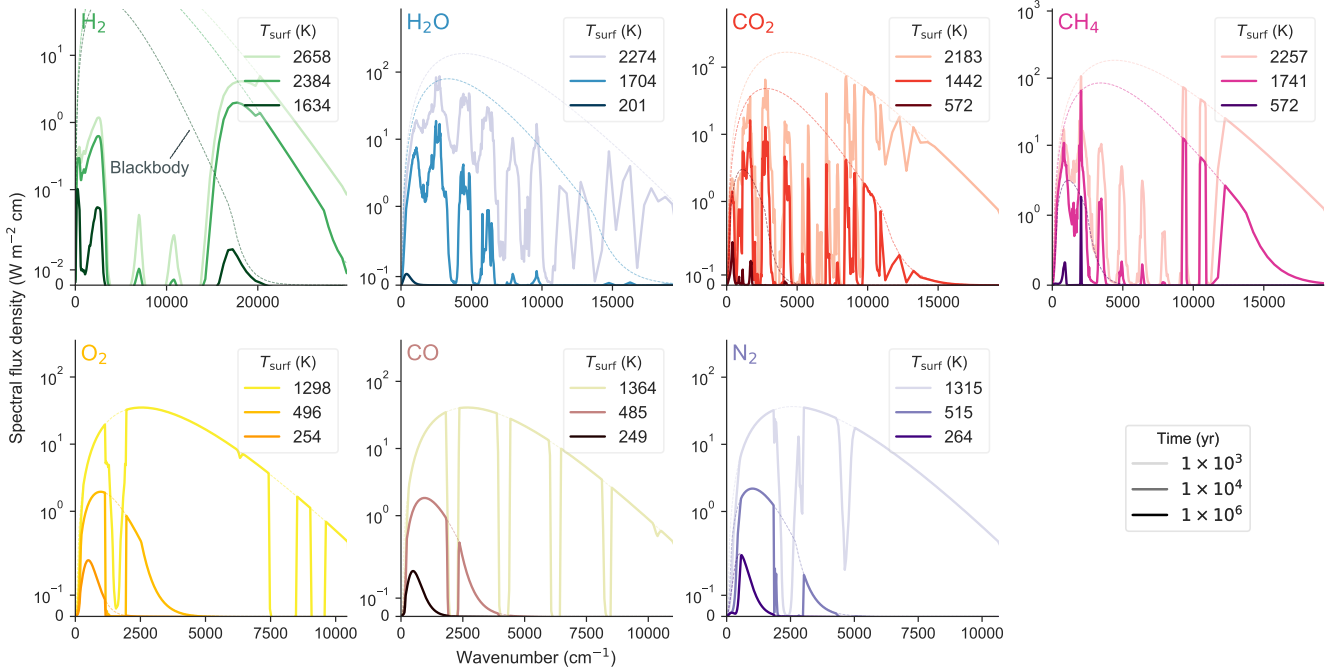


Figure 7. Top-of-atmosphere net spectral flux relative to their blackbody spectra for $t = 10^3$, 10^4 , and 10^6 yr during magma ocean evolution. These times correspond to when the rheological transition reaches the surface in the different volatile classes (Fig. 5).

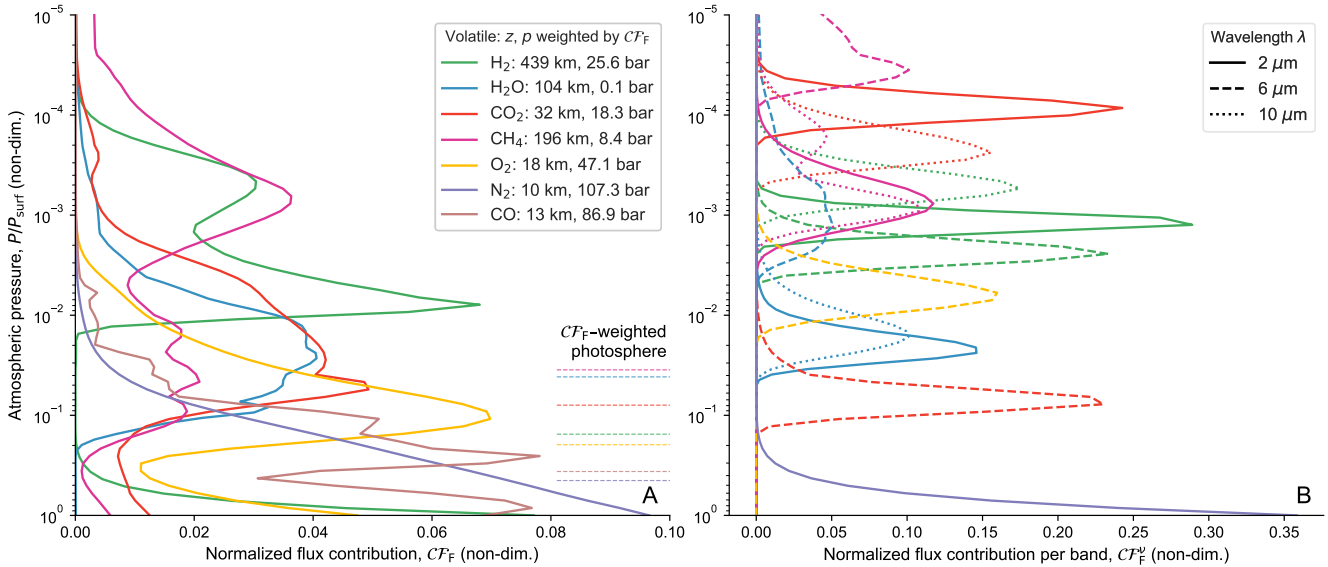


Figure 8. Total and band flux contribution from different atmospheric levels when the rheological front reaches the surface for each simulation (cf. Fig. 5). **(A)** Normalized total flux contribution. Additionally indicated are the CF_F -weighted pressure levels of the planets (*photosphere*). **(B)** Flux contribution for wavelength bands at $\lambda = 2$, 6, and 10 μm .

sure. This analysis demonstrates that we may be able to probe different layers in an atmosphere above a magma ocean (even down to the magma ocean surface) by observing planets with protoatmospheres composed of different dominant volatiles. Wavelengths exhibit different sensitivities with respect to their emitting photospheres. Fig. 8B illustrates how the primary emitting surface shifts for 2, 6, and 10 μm . For CO₂, 2 and 10 μm dominantly

probe the upper atmospheric layers, but at 6 μm deep atmospheric layers contribute most significantly to the top-of-atmosphere flux. The photosphere depth is not a linear function of wavelength but intimately tied to the opacity of the volatile and the state of the magma ocean and atmosphere. Thus, observations that exploit multiple wavelengths can uncover the thermal stratification with atmo-

spheric depths and reveal deeper or shallower parts of the temperature profile.

Figures 9 and 10 explore the sensitivity of the atmospheric state to processes that dictate the evolution of the planetary interior for the H_2O and H_2 cases. Fig. 9 shows the parameter variations we consider and illustrates how these impact evolution of the interior (see Sect. 4.3 for discussion). Figure 10 shows how the atmospheric state is perturbed based on processes operating in the interior. In general, spectral flux density variations, relative to the fiducial case, are more apparent for the H_2O case than the H_2 case. Varying the mixing length \mathcal{L}_m affects the vigor of convection in the mantle and hence leads to the strongest deviations. Solid–melt separation displays no considerable effect and inclusion of a boundary skin at the surface shows constant but small deviations by delaying cooling. An obvious feature for the H_2O case is the reduced melt fraction at the near-surface between $\approx 0\text{--}2.5$ GPa for variable \mathcal{L}_m (ii). This melt depletion of the near-surface comes with decreased surface temperature and thus muting of spectral features, most notably between $\approx 5\text{--}20 \mu\text{m}$ and up to two orders of magnitude at $\approx 6 \mu\text{m}$. At a given time, the boundary skin (iv) leads to strong enhancement of mantle melt fraction relative to the fiducial case by delaying cooling. Thus, the spectrum for this case is shifted relative to the fiducial case at a roughly similar value over all wavelengths. For the H_2 case, the difference in the spectrum is limited to the variable mixing length. Even though the total mantle melt fraction for the boundary skin case deviates even stronger from the fiducial case (relative to the H_2O deviation), there is no observable difference in the atmospheric spectrum. This is due to the strong influence of the H_2 atmosphere, which dominates the cooling rate of the planet (Fig. 5). The most notable difference between the H_2O and H_2 cases is the lower mantle melt fraction for the variable mixing length parameterization, which is depleted in melt in the H_2 case. In addition, the H_2 case with the boundary skin remains above the solidus temperature, such that the upper mantle can sustain a surface magma ocean for an extended duration relative to the fiducial case and the H_2O case. In short, processes operating in the interior can affect the spectral properties of the overlying atmosphere by up to two orders of magnitude. These are reflected by changes of the spectrum shape, features at specific wavelengths, and whole-spectrum displacements according to Wien’s law.

4. DISCUSSION

Developing the theory and models to connect astrophysical observations to the atmospheric and interior state of terrestrial planets is crucial for elevating our understanding of rocky worlds within and beyond the Solar System.

In this work we established a novel modeling framework to investigate the thermal and compositional evolution of young, rocky planets to further remove Solar System bias from considerations of early planetary evolution. In conjunction with astronomical reconnaissance of extrasolar planetary systems, this will allow to untangle the dominant physical and chemical mechanisms shaping the evolution of rocky planets from their formation to their long-term evolution. To this end, we focused on the radiative effects of varying dominant absorbers during magma ocean solidification.

4.1. Atmosphere formation & speciation

The bulk composition and eventual climate of evolved planets is a result of the physical and chemical mechanisms that operate during accretion and magma ocean evolution. We presented a modeling framework that vertically resolves the thermal structure of the planet from the core-mantle boundary at the base of the mantle to the top of the atmosphere. This will allow us in future to investigate vertical variations in mantle and atmospheric chemistry. We focused on the radiative effects of single-species atmospheres and simulated outgassing and progressing solidification, thereby establishing our coupled modeling approach as a novel tool to explore the early evolution of rocky planets. Our results highlight that various classes of cooling behavior can be expected for different volatiles. However, they do not elucidate the behavior of more complex speciation that may result from changes in the fractionation pattern during volatile delivery. From that perspective, the outgassing behavior of the two contrasting N_2 cases is particularly relevant, as it highlights the difference between reduced and oxidized planetary interiors. This emphasizes that redox evolution of the planetary mantle and atmospheric speciation are tightly interconnected, as suggested by laboratory experiments (Deng et al. 2020; Grewal et al. 2020). Considering more realistic outgassing speciation as a result of the rock composition (Schaefer & Fegley 2017; Sossi & Fegley 2018; Herbort et al. 2020) is thus necessary. In addition, we here ignore the potential effects of dynamic trapping of volatiles due to inefficient melt drainage out of the freezing front during solidification (Hier-Majumder & Hirschmann 2017). By altering the outgassing pressure, enhanced volatile trapping may influence the radiating level of the planet, but is mostly confined to the early stages of rapid freezing.

The strong effects of H_2 on the thermal sequence and crystallization are striking, even with the aforementioned caveat that part of the upper atmosphere opacity may be overestimated in our radiative transfer calculations. To compare the different absorbers using a similar standard, we considered a thick primordial atmosphere that strongly

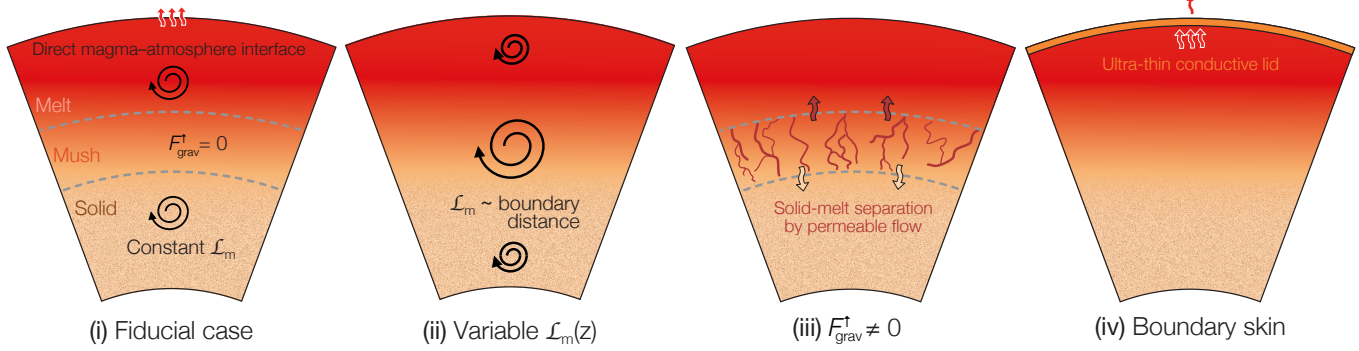


Figure 9. Illustration of interior model parameterizations and influence on mantle solidification. (i) The fiducial case with constant mixing length approximates 0-D approaches based on boundary layer theory and no separation of melt and solid occurs. Other cases relax an assumption: (ii) Mixing length \mathcal{L}_m scales with distance to the nearest domain boundary (magma ocean–atmosphere interface or core–mantle boundary), meaning that convection is most vigorous in the mid-mantle and decays towards the boundaries. (iii) Solid and melt can separate via permeable flow. (iv) The magma ocean and atmosphere are separated by an ultra-thin (\sim cm scale) conductive boundary skin, which reduces the surface temperature relative to the interior adiabat thereby increasing the cooling time.

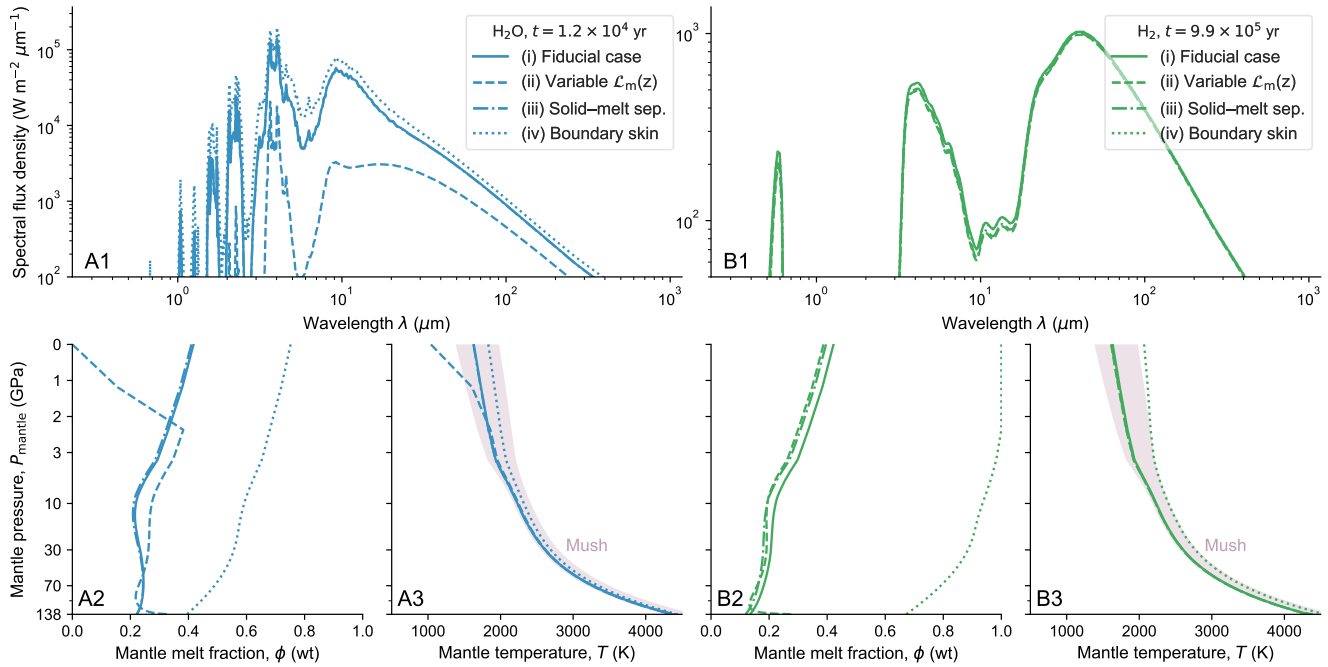


Figure 10. The influence of interior processes on spectral flux density (compare with Fig. 9), mantle melt fraction, and mantle temperature for the H_2O and H_2 cases when the rheological transition reaches the surface in the fiducial case (Fig. 5). (A) H_2O case at $t \approx 10^4$ yr, and (B) H_2 case at $t \approx 10^6$ yr. In A3 and B3 the gray area denotes the mixed region of melt and solid. Note the non-linear y-axis scale in plots A2, A3 and B2, B3. The boundary skin (iv) delays cooling and modulates the brightness temperature of a largely molten planet relative to the fiducial case.

inhibits cooling. We do not consider loss by atmospheric escape (Lammer et al. 2018; Owen 2019) and thus cannot constrain the competition between outgassing and escape. However, except for the H_2 case the short magma ocean cooling times do not allow significant time for atmospheric loss. For long-lived magma oceans, atmospheric escape could play a crucial role during the magma ocean stage of planetary evolution. Recent studies exploring the super-Earth to mini-Neptune transition argue

for a substantial influence of H_2 on the mass–radius relation due to its non-ideal partitioning into the planetary interior (Chachan & Stevenson 2018; Kite et al. 2019). Whether or not Earth-sized planets in temperate orbits can acquire substantial H_2 atmospheres remains debated, but this could alter the planetary radius if the interior remains molten due to the difference in density between molten and solid rock (Bower et al. 2019). Probing this transition with upcoming space missions will inform whether young

rocky planets experience long-lived phases of melt–solid–atmosphere interaction as we predict for the H₂ case. This will influence whether the magma ocean stage can completely overprint prior compositional variation inherited during accretion (Lichtenberg et al. 2019a).

4.2. Geophysical history of rocky exoplanets

Upcoming space missions and potentially ground-based surveys with infrared capabilities may probe the Earth-sized planetary regime on temperate orbits and will become primary tools to explore the composition and evolution of magma oceans (Lupu et al. 2014; Hamano et al. 2015; Bonati et al. 2019). We illustrate the intimate connection between interior state and atmospheric spectra, and reveal how probing different planets of different compositions can yield insights into interior processes. Planets that are dominated by atmospheric species such as N₂ or CO, or completely stripped of any atmosphere, may allow the direct observation of the planetary surface. Alternatively, the dependence of the planetary photosphere on composition and wavelength demonstrates that multi-wavelength observations may also provide opportunity to probe the temperature structure and atmospheric composition. Observations of magma oceans at different ages can reveal distinct evolutionary stages. Observations of planets around young stars can probe the fully-molten stage whereas observations of older planets reveals the sluggish phase of partial solidification; together these establish a chronology of planetary evolution. The short duration of the Earth-like cooling regime may limit the number of observational targets, depending on the age of the host star and volatile budget and composition (Bonati et al. 2019). However, planets inside the runaway greenhouse limit could offer plenty of targets with long-lived magma oceans and a wide variety of volatile inventories.

Probing the early stages of planetary evolution is relevant for the history of reduced and oxidized atmospheres. Photolysis and subsequent hydrogen escape could be a main mechanism for water depletion and oxygen build-up in rocky planetary atmospheres (Luger & Barnes 2015; Schaefer et al. 2016), and is a popular explanation to interpret exoplanetary observations in the context of planetary evolution and atmospheric composition (Kreidberg et al. 2019). However, our results illustrate that different atmospheric absorbers can produce a variety of thermal and compositional states that evolve as a planet cools, hence setting the stage for prebiotic chemical environments on young planets (Wordsworth 2012; Sasselov et al. 2020). A natural next step is to incorporate and compare the influence of additional chemical and physical processes, such as atmospheric escape (Odert et al. 2018; Wordsworth et al. 2018; Rogers & Owen 2020), chemistry (Hu et al.

2012; Pearce et al. 2020), and condensates (Marcq et al. 2017; Pluriel et al. 2019).

4.3. Interior state & tectonics

Generally speaking, we find that for all but H₂, magma ocean cooling in the Earth-type regime undergoes similar evolutionary stages as the canonical steam atmosphere: initial rapid cooling during the fully molten phase followed by a phase of more protracted cooling once the mantle reaches the rheological transition. The H₂ case, however, shows a distinct evolution with comparably protracted cooling and smoothing of the three distinct stages of solidification. In general, the different volatile cases differ by orders of magnitude with respect to the timescale of mantle crystallization. The solidification time has consequences for the compositional stratification of the post-magma ocean mantle mineralogy and style of solid-state convection (Elkins-Tanton 2008; Boukaré et al. 2015; Solomatov 2015). Fast cooling, as observed for planets with O₂, CO, and N₂ atmospheres, promotes batch crystallization of planetary mantles which decreases the tendency for compositional stratification and large-scale overturn. In contrast, more protracted cooling, which is favored for H₂, H₂O, CO₂, and CH₄ cases, promotes fractional crystallization of cumulates and thus whole mantle overturn and compositional stratification.

Furthermore, the solidification time influences the onset of solid-state convection (Ballmer et al. 2017; Maurice et al. 2017) and the intrusion efficiency of upwelling magma columns, thereby regulating the post-magma ocean cooling regime of the planet (Lourenço et al. 2018). Tidal effects due to rapid rotation following giant impacts, however, can alter the energetic balance and magmatic evolution of planetary bodies (Zahnle et al. 2015; Lock et al. 2020). From a long-term geodynamical perspective, mineralogical stratification and potential mantle overturn may result in different styles of mantle convection, separating whole-mantle convection from double-layered convection regimes with consequences for long-term outgassing behavior (Schaefer & Elkins-Tanton 2018; Spaargaren et al. 2020). In addition, we directly link the observed spectra of magma ocean planets to interior state by exploring the influence of interior processes on observables. For example, variations in the vigor of magma ocean convection are parameterized by the mixing length parameter, which is analogous to the eddy diffusivity k_{zz} in atmospheric sciences. Such modeling choices cannot be constrained by observations in the Solar System since magma oceans are no longer present, and laboratory experiments are inherently limited in parameter space. Therefore, astronomical reconnaissance of magma ocean planets may help to further constrain the relative impor-

tance of energy transfer processes operating in planetary interiors and inform appropriate parameterizations.

5. SUMMARY & CONCLUSIONS

We investigated the evolution of the interior and atmosphere of rocky planets during magma ocean solidification with a focus on the radiative effects of protoatmospheres of different composition. The newly established framework of a radiative-convective atmospheric model coupled to a vertically resolved energy balance model of the planetary mantle allows us to constrain the thermo-physical evolution of magma ocean planets from the core-mantle boundary to the top of the atmosphere. We used the radiative-convective atmosphere model to demonstrate the volatile-specific planetary cooling rate as a function of surface temperature for fixed atmospheric pressures. We then used the coupled framework to model the time-dependence of magma ocean solidification for rocky planets dominated by atmospheres comprised of H_2 , H_2O , CO_2 , CH_4 , CO , O_2 , or N_2 , finding strong variation in their thermal evolution and vertical stratification. We quantified the evolution of their atmospheric spectra and the heat flux contribution from different atmospheric levels during the evolution. This allows inferences of the interior mantle state from atmospheric signals extracted from astronomical observations. Finally, we demonstrated that the relative efficiency of energy transport by different interior processes may have a measurable effect on the associated protoatmospheres. Our coupled magma ocean–atmosphere framework thus expands the solution space in the spatial and compositional domain and makes it possible to investigate planet formation and evolution pathways that differ from the terrestrial planets in the Solar System.

Investigating magma ocean evolution with the coupled model, we find:

- The thermal sequence of magma ocean solidification is influenced by the radiatively dominant volatile to first order; cooling can be protracted by several orders of magnitude for the same orbit and planet configuration. Ordered by increasing timescale of solidification, the volatiles are grouped into three classes:
 - O_2 , N_2 , and CO are least effective as atmospheric absorbers and hence their magma oceans cool the fastest. Because of their low solubilities in silicate melts, their atmospheres form quickly to their full extent and remain at near-constant surface pressure due to their low condensation temperatures.
 - H_2O , CO_2 , and CH_4 establish an intermediate class with more protracted magma ocean cooling. Even though the tropospheric radiation

limit for the H_2O case is most pronounced, CO_2 and CH_4 show similar solidification timescales. The reason for this is a combination of their different solubilities in magma, atmospheric extinction efficiencies, and condensation temperatures.

- H_2 shows the strongest effect on extending the duration of the magma ocean phase. Even though the evolution still charts the main phases of magma ocean cooling from fully molten to partially solidified to fully solidified, the transitions between these phases are smoothed and delayed relative to the other volatiles. Solidification with an H_2 atmosphere is not completed within 100 Myr.

- Different volatile cases show different evolution of their atmospheric vertical extent because of the coupled effects of varying volatile solubility, mantle crystallization, and surface condensation.
- Magma ocean protoatmospheres show distinctive features in their spectra for different volatiles and at different times. These may guide future observations to discriminate between atmospheric primary composition and evolutionary stage.
- Spectra are further distinctive depending on interior parameterizations that alter petrological and energetic properties of magma ocean evolution. Therefore, astronomical observations of magma ocean planets may inform further understanding of the geophysical and geochemical evolution of planetary mantles and surfaces.

In conclusion, our work illustrates the importance of coupled models of rocky planetary mantles and their overlying atmospheres to reveal crucial feedback cycles that occur during early planetary evolution. Given the variety of ways to represent the physics and chemistry involved, there is a need for a range of models incorporating various aspects of the problem. We have introduced a novel model that adequately treats the primary energy transport mechanisms operating in a co-evolving planetary mantle and atmosphere. Future work will build on this modeling framework and pave the way to a more complete understanding of the environmental and surface conditions on young, rocky worlds. We anticipate that further developments—such as laboratory constraints on outgassing, atmospheric chemistry, and cloud feedbacks—will allow to simulate the extensive range of the rocky planet phase space. The insights gained through this venture will enhance our interpretation of the exoplanet census and further constrain the earliest physico-chemical conditions of our own world.

ACKNOWLEDGMENTS

The authors thank P. A. Sossi and S. P. Quanz for comments on earlier drafts, A. G. Jørgensen for providing additional line lists, L. Lichtenberg for tireless efforts in sampling petrological literature, and X. Tan, J. Wade, V. Parmentier, and R. J. Graham for discussions. This work was supported by grants from the Simons Foundation (SCOL award #611576 to T.L.), the Swiss National Science Foundation (Early Postdoc.Mobility fellowship #P2EZP2-178621 to T.L., Ambizione grant #173992 to D.J.B.), and the European Research Council (Advanced grant EXOCONDENSE #740963 to R.T.P.). DATA AVAILABILITY: The simulation data and plotting scripts to reproduce the presented findings are available at [Lichtenberg et al. \(2020a,b,c, osf.io/m4jh7\)](#). SOFTWARE: SPIDER (Bower et al. 2018), SOCRATES (Edwards & Slingo 1996), NUMPY (Harris et al. 2020; Reddy et al. 2020), SCIPY (Virtanen et al. 2020a,b), PANDAS (McKinney 2010; Reback et al. 2019), MATPLOTLIB (Hunter 2007; Caswell et al. 2019), SEABORN (Waskom et al. 2018).

APPENDIX

A. OPACITY DATA

Molecule / system	Type	ν_{\min} (cm ⁻¹)	ν_{\max} (cm ⁻¹)	Reference
H ₂ O	lbl	0	25711	Gordon et al. (2017)
H ₂ O	continuum			Mlawer et al. (2012)
CO ₂	lbl	158	140757	Gordon et al. (2017)
CO ₂ –CO ₂	CIA	1	2850	Gruszka & Borysow (1997)
H ₂ –H ₂	CIA	20	20000	Borysow et al. (2001); Borysow (2002)
CH ₄	lbl	0	11502	Gordon et al. (2017)
CH ₄ –CH ₄	CIA	1	990	Borysow & Frommhold (1987)
N ₂	lbl	12	9354	Gordon et al. (2017)
N ₂ –N ₂	CIA	0	5000	Karman et al. (2015)
O ₂	lbl	0	17272	Gordon et al. (2017)
O ₂ –O ₂	CIA	1150	29800	Baranov et al. (2004)
CO	lbl	4	1447	Gordon et al. (2017)

Table A1. List of molecules and references for the opacity data used in this work. Abbreviations: lbl – line-by-line, CIA – collision-induced absorption.

REFERENCES

- Abe, Y. 1993, In: Takahashi, E., Jeanloz, R., Rubie, D. (Eds.), *Evolution of the Earth and Planets*, Vol. 74. AGU, Washington D.C., 41, doi: [10.1029/GM074](https://doi.org/10.1029/GM074)
- . 1995, In: Yukutake, T. (Ed.), *The Earth's Central Part: Its Structure and Dynamics*. Terra Sci. Pub. Com., 215, doi: [10.1029/GM074](https://doi.org/10.1029/GM074)
- . 1997, *Phys. Earth Planet. Inter.*, 100, 27, doi: [10.1016/S0031-9201\(96\)03229-3](https://doi.org/10.1016/S0031-9201(96)03229-3)
- Abe, Y., & Matsui, T. 1986, *J. Geophys. Res.*, 91, E291, doi: [10.1029/JB091iB13p0E291](https://doi.org/10.1029/JB091iB13p0E291)
- Amundsen, D. S., Baraffe, I., Tremblin, P., et al. 2014, *A&A*, 564, A59, doi: [10.1051/0004-6361/201323169](https://doi.org/10.1051/0004-6361/201323169)
- Amundsen, D. S., Mayne, N. J., Baraffe, I., et al. 2016, *A&A*, 595, A36, doi: [10.1051/0004-6361/201629183](https://doi.org/10.1051/0004-6361/201629183)
- Andraut, D., Bolfan-Casanova, N., Nigro, G. L., et al. 2011, *Earth Planet. Sci. Lett.*, 304, 251, doi: [10.1016/j.epsl.2011.02.006](https://doi.org/10.1016/j.epsl.2011.02.006)
- Apai, D., Milster, T. D., Kim, D. W., et al. 2019, *AJ*, 158, 83, doi: [10.3847/1538-3881/ab2631](https://doi.org/10.3847/1538-3881/ab2631)
- Ardia, P., Hirschmann, M. M., Withers, A., & Stanley, B. 2013, *GeoCoA*, 114, 52
- Arnscheidt, C. W., Wordsworth, R. D., & Ding, F. 2019, *ApJ*, 881, 60, doi: [10.3847/1538-4357/ab2bf2](https://doi.org/10.3847/1538-4357/ab2bf2)
- Asplund, M., Grevesse, N., Sauval, A. J., & Scott, P. 2009, *ARA&A*, 47, 481, doi: [10.1146/annurev.astro.46.060407.145222](https://doi.org/10.1146/annurev.astro.46.060407.145222)
- Ballmer, M. D., Lourenço, D. L., Hirose, K., Caracas, R., & Nomura, R. 2017, *Geochemistry, Geophysics, Geosystems*, 18, 2785, doi: [10.1002/2017GC006917](https://doi.org/10.1002/2017GC006917)
- Baraffe, I., Chabrier, G., Allard, F., & Hauschildt, P. H. 1998, *A&A*, 337, 403. <https://arxiv.org/abs/astro-ph/9805009>
- Baraffe, I., Homeier, D., Allard, F., & Chabrier, G. 2015, *A&A*, 577, A42, doi: [10.1051/0004-6361/201425481](https://doi.org/10.1051/0004-6361/201425481)
- Baranov, Y. I., Lafferty, W. J., & Fraser, G. T. 2004, *J. Mol. Spectrosc.*, 228, 432, doi: [10.1016/j.jms.2004.04.010](https://doi.org/10.1016/j.jms.2004.04.010)
- Barth, P., Carone, L., Barnes, R., et al. 2020, *Astrobiology*, in press, arXiv:2008.09599. <https://arxiv.org/abs/2008.09599>
- Benedikt, M. R., Scherf, M., Lammer, H., et al. 2020, *Icarus*, 347, 113772, doi: [10.1016/j.icarus.2020.113772](https://doi.org/10.1016/j.icarus.2020.113772)
- Benner, S. A., Bell, E. A., Biondi, E., et al. 2019, *ChemSystemsChem*, 2, e1900035, doi: [10.1002/syst.201900035](https://doi.org/10.1002/syst.201900035)
- Bergner, J. B., Öberg, K. I., Bergin, E. A., et al. 2020, *ApJ*, 898, 97, doi: [10.3847/1538-4357/ab9e71](https://doi.org/10.3847/1538-4357/ab9e71)
- Bitsch, B., Raymond, S. N., & Izidoro, A. 2019, *A&A*, 624, A109, doi: [10.1051/0004-6361/201935007](https://doi.org/10.1051/0004-6361/201935007)

- Blank, J., Stolper, E., & Carroll, M. 1993, *Earth Planet. Sci. Lett.*, 119, 27
- Bonati, I., Lichtenberg, T., Bower, D. J., Timpe, M. L., & Quanz, S. P. 2019, *A&A*, 621, A125, doi: [10.1051/0004-6361/201833158](https://doi.org/10.1051/0004-6361/201833158)
- Borysow, A. 2002, *A&A*, 390, 779
- Borysow, A., & Frommhold, L. 1987, *ApJ*, 318, 940, doi: [10.1086/165426](https://doi.org/10.1086/165426)
- Borysow, A., Jørgensen, U. G., & Fu, Y. 2001, *J. Quant. Spectrosc. Radiat. Transf.*, 68, 235
- Boukaré, C. E., Ricard, Y., & Fiquet, G. 2015, *J. Geophys. Res. Solid Earth*, 120, 6085, doi: [10.1002/2015JB011929](https://doi.org/10.1002/2015JB011929)
- Bower, D. J., Kitzmann, D., Wolf, A. S., et al. 2019, *A&A*, 631, A103, doi: [10.1051/0004-6361/201935710](https://doi.org/10.1051/0004-6361/201935710)
- Bower, D. J., Sanan, P., & Wolf, A. S. 2018, *Phys. Earth Planet. Inter.*, 274, 49, doi: [10.1016/j.pepi.2017.11.004](https://doi.org/10.1016/j.pepi.2017.11.004)
- Caswell, T. A., Droettboom, M., Hunter, J., et al. 2019, *matplotlib/matplotlib: REL: v3.1.1, v3.1.1*, Zenodo, doi: [10.5281/zenodo.3264781](https://doi.org/10.5281/zenodo.3264781)
- Chachan, Y., & Stevenson, D. J. 2018, *ApJ*, 854, 21, doi: [10.3847/1538-4357/aaa459](https://doi.org/10.3847/1538-4357/aaa459)
- Chase Jr, M. W. 1998, *J. Phys. Chem. Ref. Data, Monograph*, 9, 1
- Chidester, B. A., Rahman, Z., Richter, K., & Campbell, A. J. 2017, *GeoCoA*, 199, 1, doi: [10.1016/j.gca.2016.11.035](https://doi.org/10.1016/j.gca.2016.11.035)
- Cox, J., Wagman, D., & Medvedev, V. 1984, *Hemisphere Publishing Corp.*, New York
- Cronin, T. W. 2014, *J. Atmos. Sci.*, 71, 2994, doi: [10.1175/JAS-D-13-0392.1](https://doi.org/10.1175/JAS-D-13-0392.1)
- Dalou, C., Hirschmann, M. M., von der Handt, A., Mosenfelder, J., & Armstrong, L. S. 2017, *Earth Planet. Sci. Lett.*, 458, 141
- Deng, J., Du, Z., Karki, B. B., Ghosh, D. B., & Lee, K. K. M. 2020, *Nat. Commun.*, 11, 2007, doi: [10.1038/s41467-020-15757-0](https://doi.org/10.1038/s41467-020-15757-0)
- Denman, T. R., Leinhardt, Z. M., Carter, P. J., & Mordasini, C. 2020, *MNRAS*, 496, 1166, doi: [10.1093/mnras/staa1623](https://doi.org/10.1093/mnras/staa1623)
- Dixon, J. E., Stolper, E. M., & Holloway, J. R. 1995, *J. Petrol.*, 36, 1607
- Dreizler, S., Jeffers, S. V., Rodríguez, E., et al. 2020, *MNRAS*, 493, 536, doi: [10.1093/mnras/staa248](https://doi.org/10.1093/mnras/staa248)
- Drążkowska, J., & Dullemond, C. P. 2018, *A&A*, 614, A62, doi: [10.1051/0004-6361/201732221](https://doi.org/10.1051/0004-6361/201732221)
- Drummond, B., Mayne, N. J., Manners, J., et al. 2018, *ApJ*, 869, 28, doi: [10.3847/1538-4357/aaeb28](https://doi.org/10.3847/1538-4357/aaeb28)
- Edwards, J. M., & Slingo, A. 1996, *Quarterly Journal of the Royal Meteorological Society*, 122, 689, doi: [10.1002/qj.49712253107](https://doi.org/10.1002/qj.49712253107)
- Eistrup, C., Walsh, C., & van Dishoeck, E. F. 2018, *A&A*, 613, A14, doi: [10.1051/0004-6361/201731302](https://doi.org/10.1051/0004-6361/201731302)
- Elkins-Tanton, L. T. 2008, *Earth Planet. Sci. Lett.*, 271, 181
- Elkins-Tanton, L. T. 2011, *Ap&SS*, 332, 359, doi: [10.1007/s10509-010-0535-3](https://doi.org/10.1007/s10509-010-0535-3)
- . 2012, *Annu. Rev. Earth Planet. Sci.*, 40, 113, doi: [10.1146/annurev-earth-042711-105503](https://doi.org/10.1146/annurev-earth-042711-105503)
- Fegley Jr., B., Lodders, K., & Jacobson, N. S. 2020, *Geochemistry*, doi: [10.1016/j.chemer.2019.125594](https://doi.org/10.1016/j.chemer.2019.125594)
- Fischer, R. A., Cottrell, E., Hauri, E., Lee, K. K. M., & Le Voyer, M. 2020, *Proc. Nat. Acad. Sci. USA*, 117, 8743, doi: [10.1073/pnas.1919930117](https://doi.org/10.1073/pnas.1919930117)
- Forget, F., & Pierrehumbert, R. T. 1997, *Science*, 278, 1273, doi: [10.1126/science.278.5341.1273](https://doi.org/10.1126/science.278.5341.1273)
- Fulton, B. J., Petigura, E. A., Howard, A. W., et al. 2017, *AJ*, 154, 109, doi: [10.3847/1538-3881/aa80eb](https://doi.org/10.3847/1538-3881/aa80eb)
- Gaillard, F., & Scaillet, B. 2014, *Earth Planet. Sci. Lett.*, 403, 307, doi: [10.1016/j.epsl.2014.07.009](https://doi.org/10.1016/j.epsl.2014.07.009)
- Gaillard, F., Schmidt, B., Mackwell, S., & McCammon, C. 2003, *GeoCoA*, 67, 2427
- Gardner, J. E., Hilton, M., & Carroll, M. R. 1999, *Earth Planet. Sci. Lett.*, 168, 201
- Gaudi, B. S., Seager, S., Mennesson, B., et al. 2020, *arXiv e-prints*, arXiv:2001.06683, <https://arxiv.org/abs/2001.06683>
- Girardi, L., Bressan, A., Bertelli, G., & Chiosi, C. 2000, *A&AS*, 141, 371, doi: [10.1051/aas:2000126](https://doi.org/10.1051/aas:2000126)
- Goldblatt, C., Robinson, T. D., Zahnle, K. J., & Crisp, D. 2013, *Nat. Geosci.*, 6, 661, doi: [10.1038/ngeo1892](https://doi.org/10.1038/ngeo1892)
- Goody, R., West, R., Chen, L., & Crisp, D. 1989, *JQSRT*, 42, 539, doi: [10.1016/0022-4073\(89\)90044-7](https://doi.org/10.1016/0022-4073(89)90044-7)
- Gordon, I. E., Rothman, L. S., Hill, C., et al. 2017, *JQSRT*, 203, 3, doi: [10.1016/j.jqsrt.2017.06.038](https://doi.org/10.1016/j.jqsrt.2017.06.038)
- Grewal, D. S., Dasgupta, R., & Farnell, A. 2020, *GeoCoA*, 280, 281, doi: [10.1016/j.gca.2020.04.023](https://doi.org/10.1016/j.gca.2020.04.023)
- Gruszka, M., & Borysow, A. 1997, *Icarus*, 129, 172, doi: [10.1006/icar.1997.5773](https://doi.org/10.1006/icar.1997.5773)
- Hamano, K., Abe, Y., & Genda, H. 2013, *Nature*, 497, 607, doi: [10.1038/nature12163](https://doi.org/10.1038/nature12163)
- Hamano, K., Kawahara, H., Abe, Y., Onishi, M., & Hashimoto, G. L. 2015, *ApJ*, 806, 216, doi: [10.1088/0004-637X/806/2/216](https://doi.org/10.1088/0004-637X/806/2/216)
- Harris, C. R., Jarrod Millman, K., van der Walt, S. J., et al. 2020, *Nature*, 585, 357. <https://arxiv.org/abs/2006.10256>
- Herbort, O., Woitke, P., Helling, C., & Zerkle, A. 2020, *A&A*, 636, A71, doi: [10.1051/0004-6361/201936614](https://doi.org/10.1051/0004-6361/201936614)
- Herzberg, C., & Zhang, J. 1996, *J. Geophys. Res.*, 101, 8271, doi: [10.1029/96JB00170](https://doi.org/10.1029/96JB00170)
- Hier-Majumder, S., & Hirschmann, M. M. 2017, *Geochemistry, Geophysics, Geosystems*, 18, 3078, doi: [10.1002/2017GC006937](https://doi.org/10.1002/2017GC006937)
- Hirschmann, M. M. 2012, *Earth Planet. Sci. Lett.*, 341, 48, doi: [10.1016/j.epsl.2012.06.015](https://doi.org/10.1016/j.epsl.2012.06.015)

- Hirschmann, M. M., Withers, A., Ardia, P., & Foley, N. 2012, *Earth Planet. Sci. Lett.*, 345, 38
- Holtz, F., Behrens, H., Dingwell, D. B., & Johannes, W. 1995, *American Mineralogist*, 80, 94
- Hu, R., Seager, S., & Bains, W. 2012, *ApJ*, 761, 166, doi: [10.1088/0004-637X/761/2/166](https://doi.org/10.1088/0004-637X/761/2/166)
- Hunter, J. D. 2007, *Comput. Sci. Eng.*, 9, 90
- Ikoma, M., Elkins-Tanton, L., Hamano, K., & Suckale, J. 2018, *SSRv*, 214, 76, doi: [10.1007/s11214-018-0508-3](https://doi.org/10.1007/s11214-018-0508-3)
- Jin, S., Mordasini, C., Parmentier, V., et al. 2014, *ApJ*, 795, 65, doi: [10.1088/0004-637X/795/1/65](https://doi.org/10.1088/0004-637X/795/1/65)
- Jontof-Hutter, D. 2019, *Annu. Rev. Earth Planet. Sci.*, 47, 141, doi: [10.1146/annurev-earth-053018-060352](https://doi.org/10.1146/annurev-earth-053018-060352)
- Journaux, B., Kalousová, K., Sotin, C., et al. 2020, *SSRv*, 216, 7, doi: [10.1007/s11214-019-0633-7](https://doi.org/10.1007/s11214-019-0633-7)
- Karman, T., Miliordos, E., Hunt, K. L. C., Groenenboom, G. C., & van der Avoird, A. 2015, *JChPh*, 142, 084306, doi: [10.1063/1.4907917](https://doi.org/10.1063/1.4907917)
- Katyal, N., Nikolaou, A., Godolt, M., et al. 2019, *ApJ*, 875, 31, doi: [10.3847/1538-4357/ab0d85](https://doi.org/10.3847/1538-4357/ab0d85)
- Kegerreis, J. A., Eke, V. R., Catling, D. C., et al. 2020, arXiv e-prints, arXiv:2007.04321, <https://arxiv.org/abs/2007.04321>
- Keppler, H., & Golabek, G. 2019, *Geochem. Perspect. Lett.*, 11, 12
- Kite, E. S., & Barnett, M. 2020, *Proc. Natl. Acad. Sci.*, 117, 18264, doi: [10.1073/pnas.2006177117](https://doi.org/10.1073/pnas.2006177117)
- Kite, E. S., Fegley, Bruce, J., Schaefer, L., & Ford, E. B. 2019, *ApJL*, 887, L33, doi: [10.3847/2041-8213/ab59d9](https://doi.org/10.3847/2041-8213/ab59d9)
- Kite, E. S., & Ford, E. B. 2018, *ApJ*, 864, 75, doi: [10.3847/1538-4357/aad6e0](https://doi.org/10.3847/1538-4357/aad6e0)
- Koll, D. D. B., & Cronin, T. W. 2019, *ApJ*, 881, 120, doi: [10.3847/1538-4357/ab30c4](https://doi.org/10.3847/1538-4357/ab30c4)
- Kopparapu, R. K., Ramirez, R., Kasting, J. F., et al. 2013, *ApJ*, 765, 131, doi: [10.1088/0004-637X/765/2/131](https://doi.org/10.1088/0004-637X/765/2/131)
- Kral, Q., Davoult, J., & Charnay, B. 2020, *Nat. Astron.*, doi: [10.1038/s41550-020-1050-2](https://doi.org/10.1038/s41550-020-1050-2)
- Kreidberg, L., Koll, D. D. B., Morley, C., et al. 2019, *Nature*, 573, 87, doi: [10.1038/s41586-019-1497-4](https://doi.org/10.1038/s41586-019-1497-4)
- Kuchner, M. J. 2003, *ApJL*, 596, L105, doi: [10.1086/378397](https://doi.org/10.1086/378397)
- Kurucz, R. L. 1995, CD-ROM 23, Smithsonian Astrophysical Observatory
- Lammer, H., Zerkle, A. L., Gebauer, S., et al. 2018, *A&A Rv*, 26, 2, doi: [10.1007/s00159-018-0108-y](https://doi.org/10.1007/s00159-018-0108-y)
- Laneuville, M., Kameya, M., & Cleaves, H. James, I. 2018, *Astrobiology*, 18, 897, doi: [10.1089/ast.2017.1700](https://doi.org/10.1089/ast.2017.1700)
- Lebrun, T., Massol, H., Chassefière, E., et al. 2013, *J. Geophys. Res. Planets*, 118, 1155
- Léger, A., Selsis, F., Sotin, C., et al. 2004, *Icarus*, 169, 499, doi: [10.1016/j.icarus.2004.01.001](https://doi.org/10.1016/j.icarus.2004.01.001)
- Li, Y., Wiedenbeck, M., Shcheka, S., & Keppler, H. 2013, *Earth Planet. Sci. Lett.*, 377, 311
- Libourel, G., Marty, B., & Humbert, F. 2003, *GeoCoA*, 67, 4123
- Lichtenberg, T., Bower, D. J., Hammond, M., et al. 2020a, Data and scripts online container for Lichtenberg et al. (2021, JGRP), OSF: osf.io/m4jh7, doi: [10.17605/osf.io/m4jh7](https://doi.org/10.17605/osf.io/m4jh7)
- . 2020b, Magma ocean simulation data for Lichtenberg et al. (2021, JGRP), figshare, doi: [10.6084/m9.figshare.13432450](https://doi.org/10.6084/m9.figshare.13432450)
- . 2020c, Plotting scripts and data for Lichtenberg et al. (2021, JGRP), Github: https://github.com/timlichtenberg/pub_21JGRP_Lichtenberg, doi: [10.5281/zenodo.4362160](https://doi.org/10.5281/zenodo.4362160)
- Lichtenberg, T., Golabek, G. J., Burn, R., et al. 2019a, *Nat. Astron.*, 3, 307, doi: [10.1038/s41550-018-0688-5](https://doi.org/10.1038/s41550-018-0688-5)
- Lichtenberg, T., Golabek, G. J., Dullemond, C. P., et al. 2018, *Icarus*, 302, 27, doi: [10.1016/j.icarus.2017.11.004](https://doi.org/10.1016/j.icarus.2017.11.004)
- Lichtenberg, T., Golabek, G. J., Gerya, T. V., & Meyer, M. R. 2016, *Icarus*, 274, 350, doi: [10.1016/j.icarus.2016.03.004](https://doi.org/10.1016/j.icarus.2016.03.004)
- Lichtenberg, T., Keller, T., Katz, R. F., Golabek, G. J., & Gerya, T. V. 2019b, *Earth Planet. Sci. Lett.*, 507, 154, doi: [10.1016/j.epsl.2018.11.034](https://doi.org/10.1016/j.epsl.2018.11.034)
- Liu, Y., Zhang, Y., & Behrens, H. 2005, *Journal of Volcanology and Geothermal Research*, 143, 219
- Lock, S. J., Stewart, S. T., & Čuk, M. 2020, *Earth Planet. Sci. Lett.*, 530, 115885, doi: [10.1016/j.epsl.2019.115885](https://doi.org/10.1016/j.epsl.2019.115885)
- Lopez, E. D., & Fortney, J. J. 2014, *ApJ*, 792, 1, doi: [10.1088/0004-637X/792/1/1](https://doi.org/10.1088/0004-637X/792/1/1)
- Lourenço, D. L., Rozel, A. B., Gerya, T., & Tackley, P. J. 2018, *Nat. Geosci.*, 11, 322, doi: [10.1038/s41561-018-0094-8](https://doi.org/10.1038/s41561-018-0094-8)
- Luger, R., & Barnes, R. 2015, *Astrobiology*, 15, 119, doi: [10.1089/ast.2014.1231](https://doi.org/10.1089/ast.2014.1231)
- Lupu, R. E., Zahnle, K. J., Marley, M. S., et al. 2014, *ApJ*, 784, 27, doi: [10.1088/0004-637X/784/1/27](https://doi.org/10.1088/0004-637X/784/1/27)
- Madhusudhan, N., Nixon, M. C., Welbanks, L., Piette, A. A. A., & Booth, R. A. 2020, *ApJL*, 891, L7, doi: [10.3847/2041-8213/ab7229](https://doi.org/10.3847/2041-8213/ab7229)
- Marcq, E., Salvador, A., Massol, H., & Davaille, A. 2017, *J. Geophys. Res. Planets*, 122, 1539, doi: [10.1002/2016JE005224](https://doi.org/10.1002/2016JE005224)
- Massol, H., Hamano, K., Tian, F., et al. 2016, *SSRv*, 205, 153, doi: [10.1007/s11214-016-0280-1](https://doi.org/10.1007/s11214-016-0280-1)
- Matsui, T., & Abe, Y. 1986a, *Nature*, 322, 526, doi: [10.1038/322526a0](https://doi.org/10.1038/322526a0)
- . 1986b, *Nature*, 319, 303, doi: [10.1038/319303a0](https://doi.org/10.1038/319303a0)
- Maurice, M., Tosi, N., Samuel, H., et al. 2017, *J. Geophys. Res. Planets*, 122, 577, doi: [10.1002/2016JE005250](https://doi.org/10.1002/2016JE005250)
- McDonough, W. F., & Sun, S. s. 1995, *Chemical Geology*, 120, 223, doi: [10.1016/0009-2541\(94\)00140-4](https://doi.org/10.1016/0009-2541(94)00140-4)
- McKinney, W. 2010, in *Proceedings of the 9th Python in Science Conference*, ed. S. van der Walt & J. Millman, 51–56

- Meixner, M., Cooray, A., Leisawitz, D., et al. 2019, arXiv e-prints, arXiv:1912.06213. <https://arxiv.org/abs/1912.06213>
- Miller-Ricci, E., Meyer, M. R., Seager, S., & Elkins-Tanton, L. 2009, *ApJ*, 704, 770, doi: [10.1088/0004-637X/704/1/770](https://doi.org/10.1088/0004-637X/704/1/770)
- Mlawer, E. J., Payne, V. H., Moncet, J. L., et al. 2012, *Philos. Trans. Royal Soc. A*, 370, 2520, doi: [10.1098/rsta.2011.0295](https://doi.org/10.1098/rsta.2011.0295)
- Moore, G., & Carmichael, I. 1998, *Contrib. Mineral. Petrol.*, 130, 304
- Mosenfelder, J. L., Asimow, P. D., Frost, D. J., Rubie, D. C., & Ahrens, T. J. 2009, *J. Geophys. Res. Solid Earth*, 114, B01203, doi: [10.1029/2008JB005900](https://doi.org/10.1029/2008JB005900)
- Mosenfelder, J. L., Von Der Handt, A., Füre, E., et al. 2019, *American Mineralogist: Journal of Earth and Planetary Materials*, 104, 31
- Mysen, B. O., Arculus, R., & Eggler, D. H. 1975, *Contrib. Mineral. Petrol.*, 53, 227
- Nakajima, S., Hayashi, Y.-Y., & Abe, Y. 1992, *J. Atmos. Sci.*, 49, 2256, doi: [10.1175/1520-0469\(1992\)049<2256:ASOTGE>2.0.CO;2](https://doi.org/10.1175/1520-0469(1992)049<2256:ASOTGE>2.0.CO;2)
- Nikolaou, A., Katyal, N., Tosi, N., et al. 2019, *ApJ*, 875, 11, doi: [10.3847/1538-4357/ab08ed](https://doi.org/10.3847/1538-4357/ab08ed)
- Noack, L., Snellen, I., & Rauer, H. 2017, *SSRv*, 212, 877, doi: [10.1007/s11214-017-0413-1](https://doi.org/10.1007/s11214-017-0413-1)
- Öberg, K. I., Murray-Clay, R., & Bergin, E. A. 2011, *ApJL*, 743, L16, doi: [10.1088/2041-8205/743/1/L16](https://doi.org/10.1088/2041-8205/743/1/L16)
- Odert, P., Lammer, H., Erkaev, N. V., et al. 2018, *Icarus*, 307, 327, doi: [10.1016/j.icarus.2017.10.031](https://doi.org/10.1016/j.icarus.2017.10.031)
- Ortenzi, G., Noack, L., Sohl, F., et al. 2020, *Sci. Rep.*, 10, 10907, doi: [10.1038/s41598-020-67751-7](https://doi.org/10.1038/s41598-020-67751-7)
- Owen, J. E. 2019, *Annu. Rev. Earth Planet. Sci.*, 47, 67, doi: [10.1146/annurev-earth-053018-060246](https://doi.org/10.1146/annurev-earth-053018-060246)
- . 2020, *MNRAS*, 495, 3160, doi: [10.1093/mnras/staa1309](https://doi.org/10.1093/mnras/staa1309)
- Owen, J. E., & Wu, Y. 2013, *ApJ*, 775, 105, doi: [10.1088/0004-637X/775/2/105](https://doi.org/10.1088/0004-637X/775/2/105)
- Pan, V., Holloway, J. R., & Hervig, R. L. 1991, *GeoCoA*, 55, 1587
- Pearce, B. K. D., Ayers, P. W., & Pudritz, R. E. 2020, *J. Phys. Chem. A*, in press, doi: [10.1021/acs.jpca.0c06804](https://doi.org/10.1021/acs.jpca.0c06804)
- Peslier, A., Schönbachler, M., Busemann, H., & Karato, S.-I. 2018, *Space Sci. Rev.*, 212, 743
- Pierrehumbert, R. T. 2010, *Principles of Planetary Climate*
- Pierrehumbert, R. T., & Gaidos, E. 2011, *ApJL*, 734, L13, doi: [10.1088/2041-8205/734/1/L13](https://doi.org/10.1088/2041-8205/734/1/L13)
- Pierrehumbert, R. T., & Hammond, M. 2019, *Annual Review of Fluid Mechanics*, 51, 275, doi: [10.1146/annurev-fluid-010518-040516](https://doi.org/10.1146/annurev-fluid-010518-040516)
- Pluriel, W., Marcq, E., & Turbet, M. 2019, *Icarus*, 317, 583, doi: [10.1016/j.icarus.2018.08.023](https://doi.org/10.1016/j.icarus.2018.08.023)
- Quanz, S. P., Absil, O., Angerhausen, D., et al. 2019, arXiv e-prints, arXiv:1908.01316. <https://arxiv.org/abs/1908.01316>
- Quintana, E. V., Barclay, T., Borucki, W. J., Rowe, J. F., & Chambers, J. E. 2016, *ApJ*, 821, 126, doi: [10.3847/0004-637X/821/2/126](https://doi.org/10.3847/0004-637X/821/2/126)
- Reback, J., McKinney, W., den Bossche, J. V., et al. 2019, *pandas-dev/pandas: v0.25.2, v0.25.2*, Zenodo, doi: [10.5281/zenodo.3509135](https://doi.org/10.5281/zenodo.3509135)
- Reddy, A., Subramanian, A., Larrosa, A., et al. 2020, *NumPy 1.19.1, v1.19.1*, Github. <https://github.com/numpy/numpy/releases/tag/v1.19.1>
- Ricker, G. R., Winn, J. N., Vanderspek, R., et al. 2015, *Journal of Astronomical Telescopes, Instruments, and Systems*, 1, 014003, doi: [10.1117/1.JATIS.1.1.014003](https://doi.org/10.1117/1.JATIS.1.1.014003)
- Rimmer, P. B., & Rugheimer, S. 2019, *Icarus*, 329, 124, doi: [10.1016/j.icarus.2019.02.020](https://doi.org/10.1016/j.icarus.2019.02.020)
- Rogers, J. G., & Owen, J. E. 2020, arXiv e-prints, arXiv:2007.11006. <https://arxiv.org/abs/2007.11006>
- Salvador, A., Massol, H., Davaille, A., et al. 2017, *J. Geophys. Res. Planets*, 122, 1458, doi: [10.1002/2017JE005286](https://doi.org/10.1002/2017JE005286)
- Sasselov, D. D., Grotzinger, J. P., & Sutherland, J. D. 2020, *Sci. Adv.*, 6, eaax3419, doi: [10.1126/sciadv.aax3419](https://doi.org/10.1126/sciadv.aax3419)
- Sasselov, D. D., & Lecar, M. 2000, *ApJ*, 528, 995, doi: [10.1086/308209](https://doi.org/10.1086/308209)
- Schaefer, L., & Elkins-Tanton, L. T. 2018, *Philos. Trans. Royal Soc. A*, 376, 20180109, doi: [10.1098/rsta.2018.0109](https://doi.org/10.1098/rsta.2018.0109)
- Schaefer, L., & Fegley, B. J. 2007, *Icarus*, 186, 462, doi: [10.1016/j.icarus.2006.09.002](https://doi.org/10.1016/j.icarus.2006.09.002)
- . 2010, *Icarus*, 208, 438, doi: [10.1016/j.icarus.2010.01.026](https://doi.org/10.1016/j.icarus.2010.01.026)
- . 2017, *ApJ*, 843, 120, doi: [10.3847/1538-4357/aa784f](https://doi.org/10.3847/1538-4357/aa784f)
- Schaefer, L., Wordsworth, R. D., Berta-Thompson, Z., & Sasselov, D. 2016, *ApJ*, 829, 63, doi: [10.3847/0004-637X/829/2/63](https://doi.org/10.3847/0004-637X/829/2/63)
- Silver, L. A., Ihinger, P. D., & Stolper, E. 1990, *Contrib. Mineral. Petrol.*, 104, 142
- Simpson, G. C. 1929, *Q. J. R. Meteorol. Soc.*, 55, 73, doi: [10.1002/qj.49705522908](https://doi.org/10.1002/qj.49705522908)
- Solomatov, V. 2015, in *Treatise on Geophysics (Second Edition)*, 2nd edn., ed. G. Schubert (Oxford: Elsevier), 81 – 104, doi: <https://doi.org/10.1016/B978-0-444-53802-4.00155-X>
- Sossi, P. A., & Fegley, B. J. 2018, *Rev. Mineral. Geochem.*, 84, 393, doi: [10.2138/rmg.2018.84.11](https://doi.org/10.2138/rmg.2018.84.11)
- Sossi, P. A., Klemme, S., O'Neill, H. S. C., Berndt, J., & Moynier, F. 2019, *GeoCoA*, 260, 204, doi: [10.1016/j.gca.2019.06.021](https://doi.org/10.1016/j.gca.2019.06.021)
- Spaargaren, R. J., Ballmer, M. D., Bower, D. J., Dorn, C., & Tackley, P. J. 2020, arXiv e-prints, arXiv:2007.09021. <https://arxiv.org/abs/2007.09021>
- Stolper, E., & Holloway, J. R. 1988, *Earth Planet. Sci. Lett.*, 87, 397

- Stothers, R. B., & Chin, C. 1997, *Astrophys. J. Lett.*, 478, L103, doi: [10.1086/310552](https://doi.org/10.1086/310552)
- Sun, Z. 2011, *Quart. J. Roy. Meteorol. Soc.*, 137, 2138
- Takahashi, E. 1986, *J. Geophys. Res.*, 91, 9367, doi: [10.1029/JB091iB09p09367](https://doi.org/10.1029/JB091iB09p09367)
- The LUVUOIR Team. 2019, arXiv e-prints, arXiv:1912.06219. <https://arxiv.org/abs/1912.06219>
- Tikoo, S. M., & Elkins-Tanton, L. T. 2017, *Philos. Trans. Royal Soc. A*, 375, 20150394, doi: [10.1098/rsta.2015.0394](https://doi.org/10.1098/rsta.2015.0394)
- Trønnes, R. G., & Frost, D. J. 2002, *Earth and Planetary Science Letters*, 197, 117, doi: [10.1016/S0012-821X\(02\)00466-1](https://doi.org/10.1016/S0012-821X(02)00466-1)
- Turbet, M., Ehrenreich, D., Lovis, C., Bolmont, E., & Fauchez, T. 2019, *A&A*, 628, A12, doi: [10.1051/0004-6361/201935585](https://doi.org/10.1051/0004-6361/201935585)
- van 't Hoff, M. L. R., Bergin, E. A., Jørgensen, J. K., & Blake, G. A. 2020, *ApJL*, in press, arXiv:2006.12522. <https://arxiv.org/abs/2006.12522>
- Virtanen, P., Gommers, R., Oliphant, T. E., et al. 2020a, *Nat. Methods*, 17, 261, doi: [10.1038/s41592-019-0686-2](https://doi.org/10.1038/s41592-019-0686-2)
- Virtanen, P., Gommers, R., Burovski, E., et al. 2020b, *scipy/scipy: SciPy 1.5.2, v1.5.2, Zenodo*, doi: [10.5281/zenodo.3958354](https://doi.org/10.5281/zenodo.3958354)
- Wang, Z., Laurenz, V., Petitgirard, S., & Becker, H. 2016, *Earth Planet. Sci. Lett.*, 435, 136, doi: [10.1016/j.epsl.2015.12.012](https://doi.org/10.1016/j.epsl.2015.12.012)
- Waskom, M., Botvinnik, O., et al. 2018, *Seaborn v0.9.0*. doi.org/10.5281/zenodo.1313201
- Way, M. J., Aleinov, I., Amundsen, D. S., et al. 2017, *ApJS*, 231, 12, doi: [10.3847/1538-4365/aa7a06](https://doi.org/10.3847/1538-4365/aa7a06)
- Wiscombe, W., & Evans, J. 1977, *J. Comput. Phys.*, 24, 416
- Wolf, A. S., & Bower, D. J. 2018, *Phys. Earth Planet. Inter.*, 278, 59, doi: [10.1016/j.pepi.2018.02.004](https://doi.org/10.1016/j.pepi.2018.02.004)
- Wordsworth, R. D. 2012, *Icarus*, 219, 267, doi: [10.1016/j.icarus.2012.02.035](https://doi.org/10.1016/j.icarus.2012.02.035)
- . 2016, *Earth Planet. Sci. Lett.*, 447, 103, doi: [10.1016/j.epsl.2016.04.002](https://doi.org/10.1016/j.epsl.2016.04.002)
- Wordsworth, R. D., Kalugina, Y., Lokshtanov, S., et al. 2017, *Geophys. Res. Lett.*, 44, 665, doi: [10.1002/2016GL071766](https://doi.org/10.1002/2016GL071766)
- Wordsworth, R. D., & Pierrehumbert, R. T. 2013a, *Science*, 339, 64, doi: [10.1126/science.1225759](https://doi.org/10.1126/science.1225759)
- . 2013b, *ApJ*, 778, 154, doi: [10.1088/0004-637X/778/2/154](https://doi.org/10.1088/0004-637X/778/2/154)
- Wordsworth, R. D., Schaefer, L. K., & Fischer, R. A. 2018, *AJ*, 155, 195, doi: [10.3847/1538-3881/aab608](https://doi.org/10.3847/1538-3881/aab608)
- Yamashita, S. 1999, *J. Petrol.*, 40, 1497
- Yoshioka, T., Nakashima, D., Nakamura, T., Shcheka, S., & Keppler, H. 2019, *GeoCoA*, 259, 129
- Zahnle, K. J., & Carlson, R. W. 2020, in *Planetary Astrobiology*, University of Arizona Press, ed. V. Meadows, D. J. Des Marais, G. Arney, & B. Schmidt, 3–37
- Zahnle, K. J., Kasting, J. F., & Pollack, J. B. 1988, *Icarus*, 74, 62, doi: [10.1016/0019-1035\(88\)90031-0](https://doi.org/10.1016/0019-1035(88)90031-0)
- Zahnle, K. J., Lupu, R., Catling, D. C., & Wogan, N. 2020, *Planet. Sci. J.*, 1, 11, doi: [10.3847/PSJ/ab7e2c](https://doi.org/10.3847/PSJ/ab7e2c)
- Zahnle, K. J., Lupu, R., Dobrovolskis, A., & Sleep, N. H. 2015, *Earth Planet. Sci. Lett.*, 427, 74, doi: [10.1016/j.epsl.2015.06.058](https://doi.org/10.1016/j.epsl.2015.06.058)
- Zerr, A., Diegeler, A., & Boehler, R. 1998, *Science*, 281, 243, doi: [10.1126/science.281.5374.243](https://doi.org/10.1126/science.281.5374.243)
- Zhang, J., & Herzberg, C. 1994, *J. Geophys. Res.*, 99, 17,729, doi: [10.1029/94JB01406](https://doi.org/10.1029/94JB01406)